University of Crete - Master Program - Physics:

Photonics and Nanoelectronics

Advance electronic materials for hydrogen sensing

Master thesis of Kampitakis Viktor

Corresponding Associate: Vassilios Binas

Committee: Eleftherios Iliopoulos, George Deligiorgis, Thomas Anthopoulos

In collaboration with

FORTH
INSTITUTE OF ELECTRONIC STRUCTURE AND LASER

جامعة الملك عبدالله للعلوم والتقنية
King Abdullah University of Science and Technology

National Technical University of Athens

Abstract

The last decades research has faced a challenge to replace fossil fuels with new energy sources that are not harmful to the environment. After years of experiments this study led to believe that hydrogen gas is an excellent candidate for a renewable source of power that does not produce hazard products to the environment. Based on that belief there is a high necessity for electronic devices that can control and detect the presence of hydrogen for safety reasons. Our research is focused on the study and fabrication of low cost and low power gas sensor devices in order to detect the presence of hydrogen in different concentrations. The gas sensing element which was used for the first time for these experiments is copper thiocyanate (CuSCN) in different forms (powder, thin solid films). This study gave emphasis in multiple aspects of the material and the device for the better understanding of its gas sensing mechanisms. The results exhibited that CuSCN is an excellent candidate for hydrogen detection to low concentration limits by using low voltage and no external heat source.

Index

Chapter 1: Theory

1.1 Semiconductors

Globally, materials are subdivided in groups with common properties. One of the most important characteristics of an element is described by its electronic properties that are mostly depended from its electronic band structure. More specifically, bonds between atoms inside a material create quantum energy states which electrons can occupy and transfer. In the macroscopic scale of a pure material these states become dense and create two elementary bands, the valence band in which all states are occupied by electrons and the conduction band which contains unoccupied states that electrons from the valence band can transit when they absorb energy. The energy gap between these two bands controls the electronic properties of the material while this transition can be used to create electricity.

In that way materials can be separated in three groups, insulators, semiconductors and conductors. As Figure 1.1 explains, insulators have wide band gaps (>4 eV) which make the electronic transition very difficult while conductors have a very small band gap. In the case of semiconductors the band gap can range from 1 eV to 4 eV.

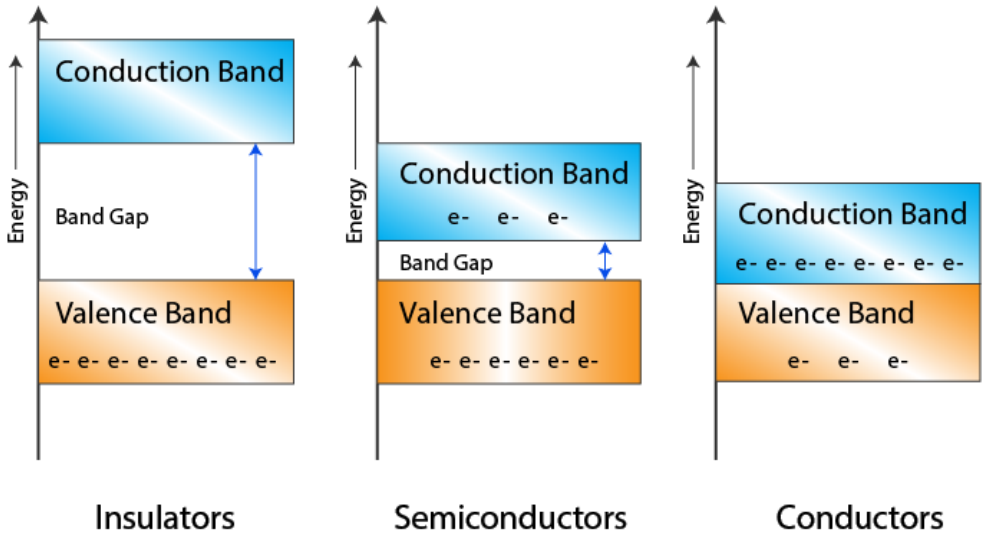

Figure 1.1: Energy band diagrams of insulators, semiconductors and conductors

Commonly, semiconductor materials have a crystal structure in which every atom has a determined position. However, in every crystal there are defects (atoms vacancies, impurities, etc) inside the structure which can alter some electronic energy states and create new states inside the band gap. The position of these states is crucial for the electronic properties of a semiconductor and thus they are used to separate the semiconductor into three types, an intrinsic semiconductor, a p-type semiconductor and an n-type semiconductor.

Figure 1.2 reveals the difference between the three types of semiconductors. Occupied defect energy states inside the band gap close to the conduction band (donor states) create an excess of electrons in the conduction band. On the other hand, unoccupied defect energy states inside the band gap and close to the valence band (acceptor states) can be easily fulfilled by electrons from the valence band. When an electron from the valence band moves into one of these states it leaves an empty spot in the valence band which can be occupied by other electrons with lower energy. This absence can be explained as positive charge (hole) moving in the opposite direction of the electrons in the energy band. The concentration of these two carriers (electrons and holes) describes the type of the semiconductor. N-type semiconductors have higher concentration of electron carriers in the conduction band than hole carriers in the valence band while the opposite phenomenon describes a p-type semiconductor. In the case of an intrinsic semiconductor hole and electrons concentrations are equal. The most common example of an intrinsic semiconductor is a semiconductor that has no defect states.

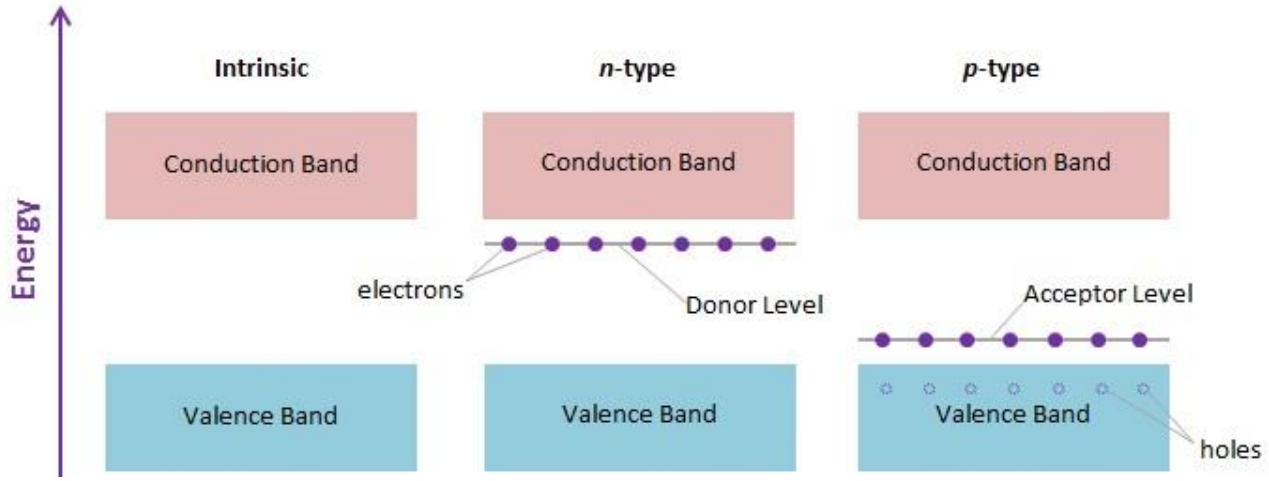

Figure 1.2: Energy band diagrams of intrinsic, n-type and p-type semiconductors.

1.2 Copper Thiocyanate

Copper thiocyanate (CuSCN) is an inorganic semiconductor which can be found in different crystal structures. Theoretical and experimental studies [1,2] have revealed that there are two phases of CuSCN with different structures, α-phase and β-phase. As presented in Figure 1.3, α-phase is related to an orthorhombic structure while β-phase has a hexagonal structure. The most common phase is β-phase while it seems to be slightly more stable.

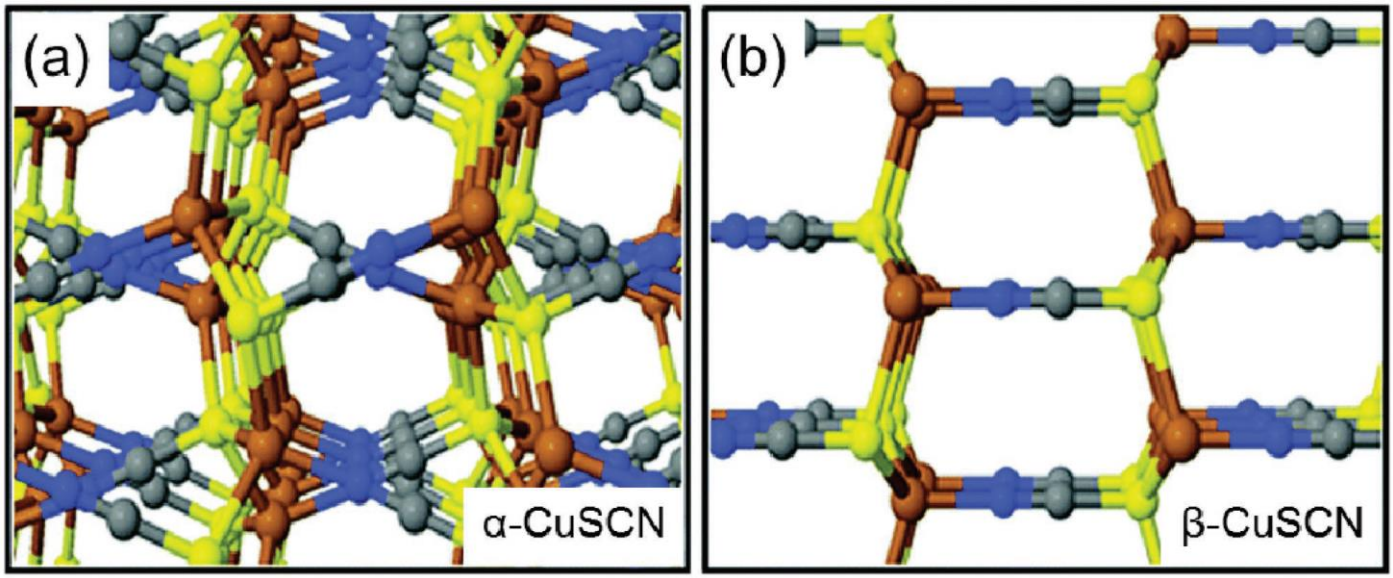

Figure 1.3: Polytypes of CuSCN structures (Cu: brown, S: yellow, C: gray, N: blue spheres). Copyright 2016, IOP Science [3].

Studies focused on the β-phase [4,5] have shown that CuSCN is a wide band gap semiconductor (>3.4 eV) with p-type characteristics. The increased hole concentration is attributed to the copper vacancies inside the crystal structure which shifts the Fermi level below the valence bands maximum. This shift attributes to the high conductance of the CuSCN element.

The wide band gap of the CuSCN and its low cost commercial availability (mostly in powder form) makes it an excellent candidate for transparent devices. Studies so far, have used CuSCN films for the development of hole transport layer (HTL) for collar cells, thin film transistors (TFTs) and other optoelectronic devices

such as organic light emitting diodes (OLEDs). However there are no references or studies in the use of CuSCN as a gas sensing element.

1.3 Conductometric gas sensors

Gas sensing devices are based on the interaction between the surface of an element and gas species on the environment, which changes different properties of the element. Conductance alternation is the most common and widely used way to detect gasses by using a semiconducting element and an input voltage.

More specifically the sensing element is deposited in substrates with interdigitated electrodes (IDEs), and placed inside a chamber which is connected with a gas line in the input and a vacuum pump in the output. The IDE is connected with a digital multimeter which is controlled from a computer. When a constant flow of mixed gasses which are controlled by mass flow controllers enter the chamber the sensing device detects the gas molecules by changing its conductivity and thus the total current shifts. Figure 1.4 shows a schematic of the basic gas sensing setup.

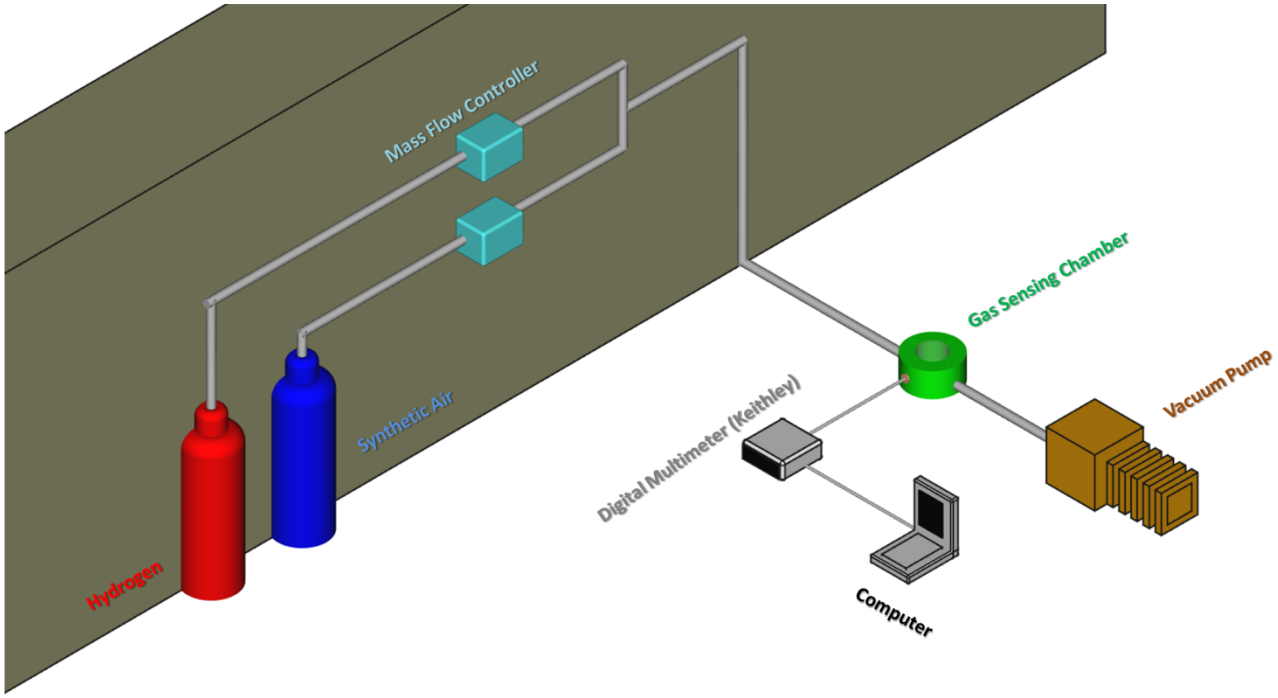

Figure 1.4: Schematic of gas sensing setup

For a complete sensing cycle, a common gas of the atmosphere such as nitrogen or synthetic air is induced inside the chamber until the current reach a constant baseline. At the next step, a pure gas is mixed with the previous one in order to achieve a desirable concentration for detection. When the current reaches a constant value, pure synthetic air or nitrogen is induced again inside the chamber in order to recover the sensor in its previous state.

The gas sensing mechanism as explained previously is based on the interaction of the gas molecules and the surface of the semiconductor, through different types of bonds. In the most cases [6], the gas molecules are adsorbed in the surface with weak energy bonds and mostly in the sites where crystal defects can be found. In that case each gas works as an oxidizing agent by trapping electrons from the conduction band or as a reducing agent by releasing electrons in the conduction band as explained in Figure 1.5. This observation leads to the belief that the type of change in the conductivity is highly depended from the type of semiconductor and the type of the gas. Table 1.1 exhibits the expected type of change in all cases of physical adsorption.

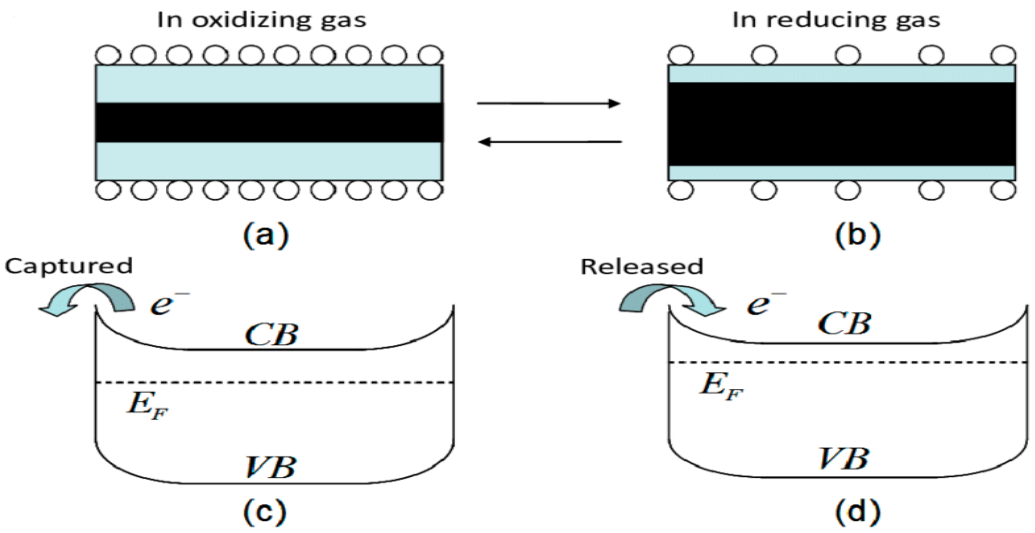

Figure 1.5: The change of electron concentration in the conduction band through the adsorption of (a), (c) an oxidizing gas and (b), (d) a reducing gas. Copyright 2014, MDPI [7].

Table 1.1: Types of change in the conductivity in the different type of semiconductors and gasses respectively

Type of gas	n-type semiconductor	p-type semiconductor
Oxidizing	Increased conductivity	Decreased conductivity
Reducing	Decreased conductivity	Increased conductivity

The efficiency of a gas sensor is measured by multiple factors, although it's established that the primary factors are sensitivity, stability, and selectivity. Moreover, sensitivity is measured by the **response** of the sensor in the tested gas concentration while the formulas to measure that response depend by the type of change in the total current which is presented bellow in the equations (1) and (2). The **stability** of the sensor expresses how stable is the sensor's efficiency after long time periods while the **selectivity** indicates the highest performance of the sensor in a specific targeted gas.

$$\mathbf{R} = \frac{(Igas - Iair)}{Iair}\,\mathbf{100\%} \qquad \textbf{when } \mathbf{I_{gas} > I_{air}} \qquad \textbf{(1)}$$

$$\mathbf{R} = \frac{(Iair - Igas)}{Igas}\,\mathbf{100\%} \qquad \textbf{when } \mathbf{I_{air} > I_{gas}} \qquad \textbf{(2)}$$

Where R is the response, I_{air} is current when the sensors are exposed to synthetic air (or nitrogen) and I_{gas} is the current when the sensor is exposed to the targeted gas.

However, there are more factors to be considered such as **response** and **recovery** time in order to develop high performance sensors. Additionally, the working temperature of the sensor is of great importance while it controls the reactivity of interactions between the gas molecules and the semiconductor's surface, as also the type of interaction between them. As a well-known example [8], the type of oxygen species adsorbed on the surface of metal oxides is dependent on the operating temperature. More specifically, oxygen species interact with a simple absorption mechanism in the vicinity of defects on the surface which are created by oxygen vacancies of the material by abstracting electrons from the sensor surface as O_2^- (>100 ^oC), O^-

(100–300 ºC) and O^{2-}(>300 ºC). Nonetheless, the interaction between oxygen species and thiocyanate based materials is not revealed yet.

1.4 Hydrogen detection

Hydrogen is a colorless, odorless, tasteless, non-toxic, nonmetallic, highly combustible diatomic gas with the molecular formula H_2. Since it consisted by two hydrogen atoms, hydrogen molecule is considered to be the smallest and lightest molecule existing, with a molecular weight of 2.016 g/mol and a radius of 1,5 Å. In its gaseous form, hydrogen is acting as a reducing agent while it forms explosive mixtures with air in concentrations from 4–75% which can be triggered by spark, heat, or sunlight. For these reasons the threshold limit value (TLV) of hydrogen concentration for safety use is considered to be **5000 ppm**.

Subsequently, the detection of Hydrogen (H_2) is of great importance, due to its use to a numerous of applications, mainly in the field of energy [9]. In the last decade hydrogen economy has been strongly emerged in order to phase out fossil fuels and contribute to global warming solutions while the reactions produce lower amount of carbon based byproducts than fossil fuels. In addition there is a high demand for advanced research and development in several fields of hydrogen production such as water splitting [10] through power to gas (P2G) conversion which does not include carbon elements. Moreover, multiple hydrogen fuel cells [11,12] have been virally tested for energy conversion and storage through hydrogen and oxygen reactions while different mechanisms for this energy market have been proposed such as peer to peer (P2P) community [13]. Furthermore, the commercial use of hydrogen as a fuel has already been used from the automobiles industries [14,15] by utilizing high pressure hydrogen gas tanks based on carbon-composite technologies [16], and it's expected to be used in several more power related industries. Nevertheless, in all fields the using of hydrogen must be extremely cautious while in high concentrations in the range of 4%-75% in the presence of air hydrogen becomes extremely flammable and auto-ignites [17]. Therefore, in order to achieve an effective power grid it is imperative to develop and establish low cost and low power hydrogen sensors in both high and low concentrations for safety and control reasons. Various metal oxides semiconductors such as n-type SnO_2[18,19], ZnO [20,21], TiO_2[22] and p-type CuO [23], NiO [24] have

been reported to be sensitive to hydrogen, yet only a few of them can be functional in room temperature and use low input voltage due to their low conductivity.

In previous studies, Lupan et all [21] developed hydrogen nanosensor by using a single nanowire (NW) of ZnO modified with Pd nanoparticles via electrochemical deposition exhibiting a tremendous response of 13100 in 100 ppm of hydrogen at room temperature. However, the recovery of the sensor is questionable while the current seems not to recover completely. Additionally, Jae-Hum Kim [18] used a vapor-liquid-solid technique in order to fabricate $Sn0_2$ NWs and decorated them Pd particles with a UV reduction. The sensor exhibited a great response of 28 ($R=\frac{Rgas}{Rair}$) in a hydrogen concentration of 100 ppm at an operating temperature of 300^{o}C.

The power consumption is also of a great importance when it comes to the use of hydrogen sensors in microelectromechanical systems (MEMS) and chips. Most studies on hydrogen microsensors exhibit a necessary power consumption in the range of 10-100 mWatts in order to function properly with a low background noise [25–27]. These values cannot further decrease due to the high voltage power (1 - 10 Volts) that is needed as also the high working temperatures that requires the use of a microheater.

In this work, different solution based CuSCN hydrogen sensors were fabricated by utilizing low cost techniques such as drop casting and spin coating. All sensors exhibited high responses in the presence of low concentrations of hydrogen (200-1000 ppm) with no external heating sources, while the power consumptions were ranging in few μWatts. Furthermore, Density Functional Theory (DFT) calculations have been utilized in order to study the interaction between hydrogen species and the β-phase of CuSCN.

Chapter 2: Development and Deposition

Conductometric gas sensor devices are based on three fundamental parts, the interdigitated electrodes (IDEs), the sensing element which is deposited on top or under the IDEs and the substrate. In this research the sensing element is placed on top of the IDEs which were deposited on glass substrates.

2.1 IDEs Fabrication

Based on the commercial IDEs of DropSens, we developed our IDEs via lithography and metal evaporation technique. More specifically, photoresist was deposited on top of fused silica glasses with spin casting, and was exposed at UV-light by using a pre-patterned mask. The exposed areas of the photoresist were dissolved by using potassium hydroxide (KOH) and the substrates were placed inside a thermal evaporator chamber in order to deposit layers of metal. After that, the rest of the photoresist was dissolved by using acetone. As a result a patterned metal layer was left on the top of the fused silica. The complete procedure is presented in the Figure 2.1 bellow.

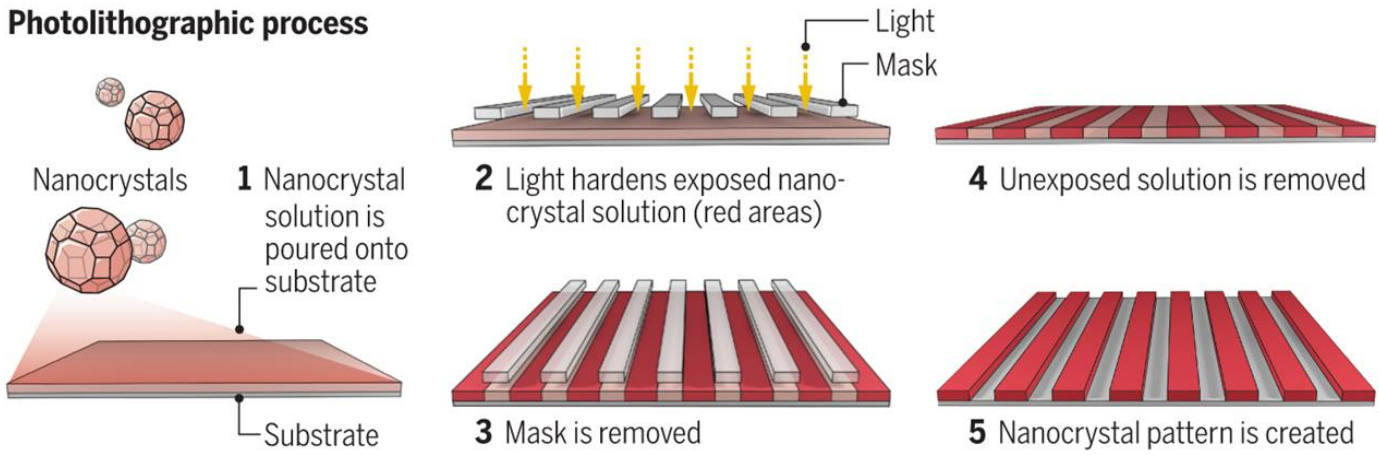

Figure 2.1: Illustration of the photolithography technique used for the development of the IDEs. Copyright 2017, American Association for the Advancement of Science [28].

Regarding to the geometry of the pattern, all IDEs contain 2 x 250 digits (electrodes) with a digit width of 5 um while the gap between them was at a constant value of 5 um. In order to optimize the device's

performance and understand the sensing mechanisms, IDEs with gold, platinum and palladium electrodes were fabricated, while they are widely known for their catalytic properties as noble metals which can enhance the sensor's sensitivity towards hydrogen gas.

2.2 Powder Deposition

CuSCN gas sensing elements in the form of powder were deposited on top of the 5 μm IDEs by using a simple drop casting technique. More specifically, CuSCN was dispersed in methanol in a ratio of 1:5 mg/mL and was sonicated for 15 minutes to dismantle the agglomerated big grains into smaller grains. Shortly after the sonication, the mixture was deposited on the IDEs via a single drop casting technique and left under a hood overnight to evaporate the methanol in a room temperature. As a result, CuSCN grains form paths that connect the neighboring electrodes with a uniform surface, as shown in the Figure 2.2 bellow.

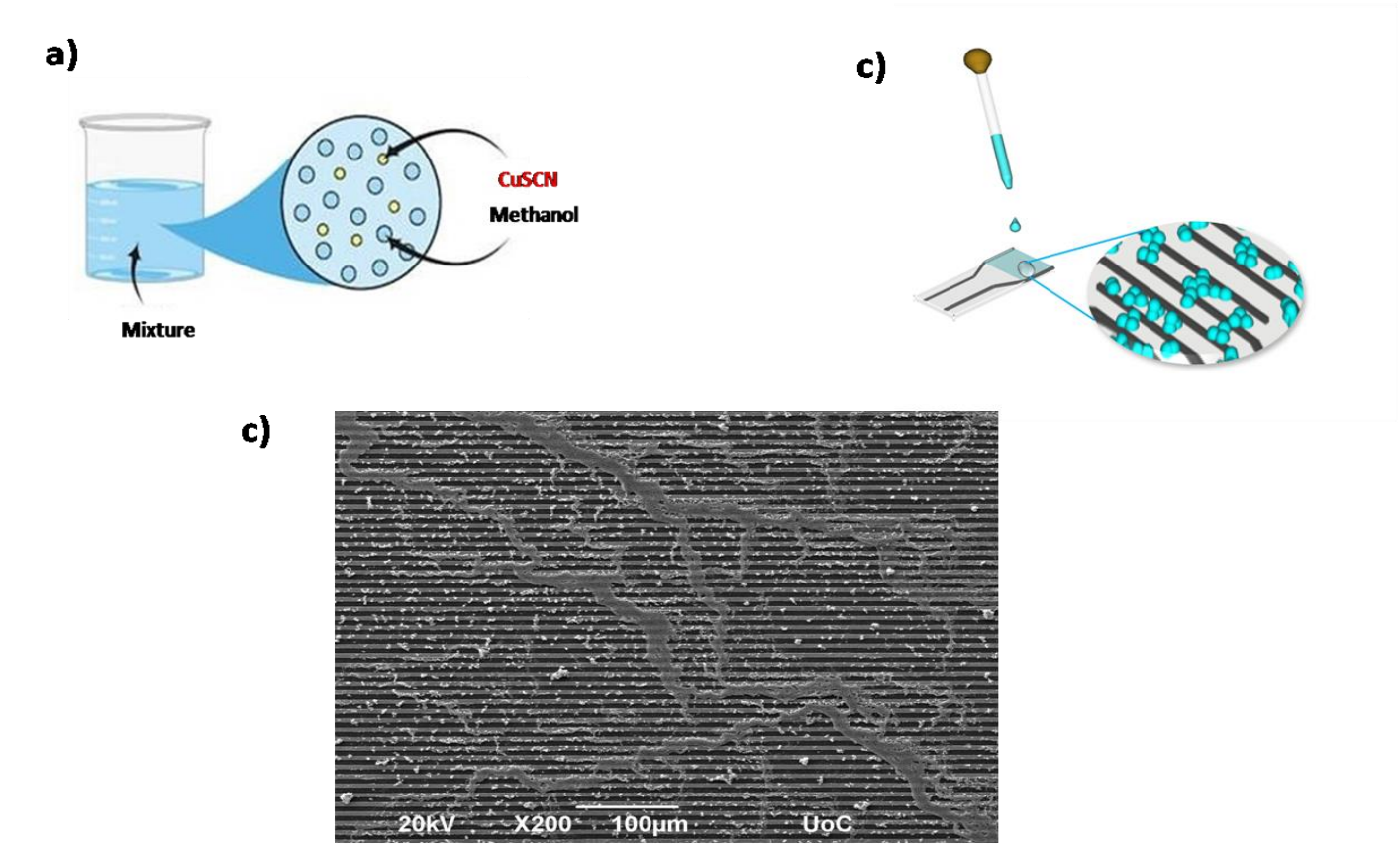

Figure 2.2: Illustration of a) the CuSCN/Methanol mixture, b) the drop casted powder on top of the IDE, c) SEM image of CuSCN powder sensor

2.3 Ink Development

Due to its low solubility, CuSCN can be diluted only in a few solvents. Previous studies [5],[29] reports that aqueous Ammonia (NH_4OH) and Diethyl Sulfide (DES) can be used as functional solvents in order to develop thin films of CuSCN in all types of substrates by utilizing the spin coating technique.

In this work, we developed two different solutions with the same concentration of CuSCN. Following the previous studies, we dissolved CuSCN powder purchased by Sigma-Aldrich in aqueous ammonia (25%) and in diethyl sulfide, with a CuSCN concentration of 25mg/mL. In both cases the solutions were stirred for one hour in temperatures of 50^{o}C for the CuSCN/NH_3 solution and 100^{o}C for the CuSCN/DES solution. The different stirring temperatures were based on the best solubility of each solvent. The final solutions were left under a hood overnight to ensure that the system has reached thermal equilibrium and after were filter by using 0.45 μm nylon filters. As it can be seen in the Figure 2.3, the CuSCN/DES solution is highly transparent, while the CuSCN/NH_3 solution seems to have a deep blue color. As previous studies [5] have pointed, the deep blue color of the CuSCN/NH_3 solution reflects to the Cu^+ ions formation while ammonia dismantles the CuSCN bonds and create Cu^+ and $(SCN)^-$ ions. CuSCN bonds can be formed again even in room temperatures when ammonia evaporates.

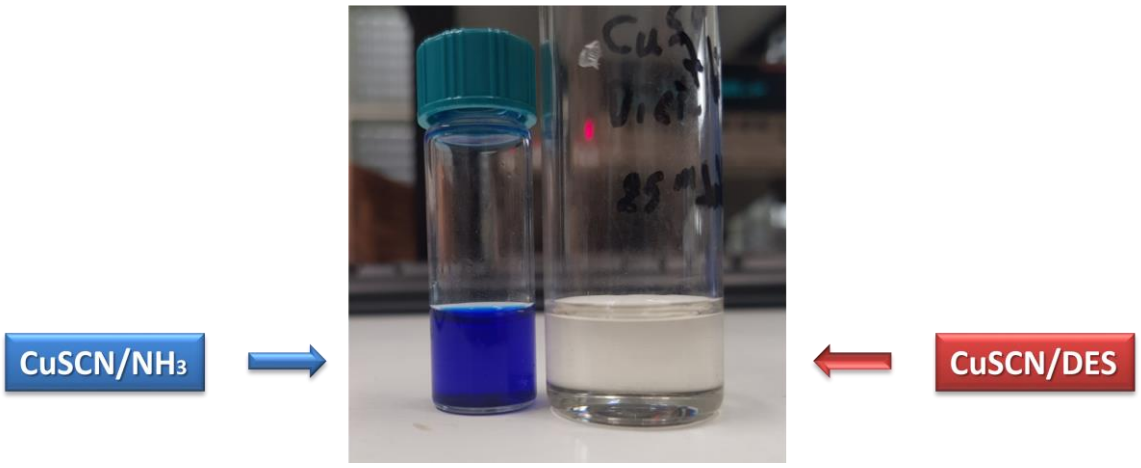

Figure 2.3: Picture of the developed CuSCN/NH_3 and CuSCN/DES solutions

2.4 Film Deposition

The prepared solutions can be used for thin film depositions through various techniques. In this work we used one of the most common techniques, the spin coating, in which few droplets of a solution are dropped on top of different substrates which are mounted on a rotated stage. When the substrates start to rotate in high speeds the droplets start to spread and create uniform layers. However, the surface tension between the substrate and the solution plays a major role in the formation of the layer, while high tensions lead to agglomeration of the droplets. For this reason, all substrates were treated under oxygen plasma in order to reduce the surface tension.

The substrates that were used for the CuSCN film deposition were fused silica glasses for the optical characterization, silicon wafers for the morphological and structural characterization and the fabricated IDEs for the sensors' development. All samples were spin casted for 60 seconds in a rotation speed of 1000 rpm and then undergo a thermal treatment in a hot plate for 20 minutes in a temperature of 100^{o}C to increase their crystallinity. Figure 2.4 shows an illustration of the developed thin films on top of the IDEs, as also a picture of the actual sensor obtained by a Field Emission Scanning Electron Microscope (FESEM).

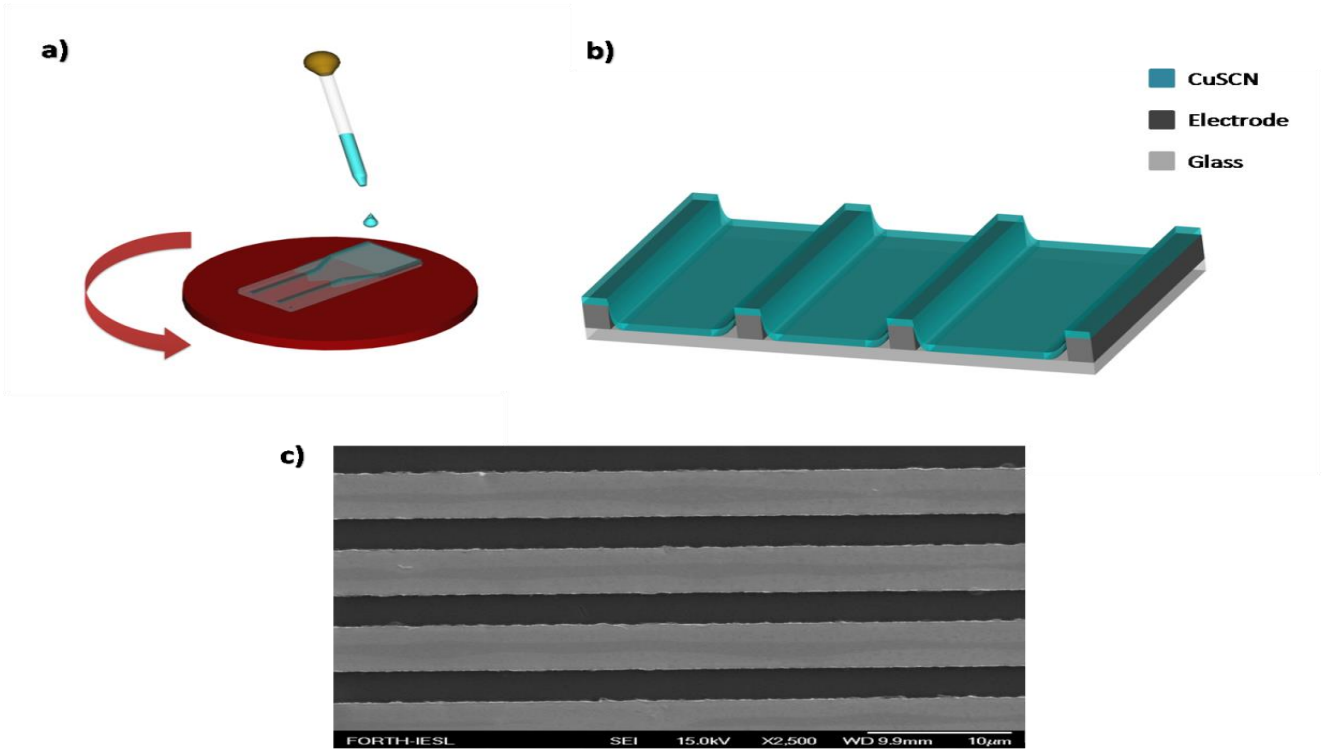

Figure 2.4: a) Spin casted CuSCN solution on top of an IDE, b) cross section of the gas sensor, c) FESEM picture of the gas sensor's surface

Chapter 3: Elements Characterization and properties

3.1 Powder Characterization

3.1.1 Structural properties

In order to confirm and analyze the structure of the CuSCN powder, X-Ray Diffraction (XRD) spectra was utilized in a wide range of diffraction angles (5^o-80^o) as it can be seen in Figure 3.1. More specifically, CuSCN powder exhibits a polycrystalline structure as it contains multiple peaks with six of them having notably higher intensities. By using X'Pert HighScore Plus software, the hexagonal β-phase crystal structure of CuSCN was confirmed through all peaks, while the six peaks with the higher intensities corresponds to the crystal planes (003), (101), (006), (104), (110) and (009) as it is presented in the Table 3.1. In addition, the crystallite size of the planes were calculated by using Scherrer's formula

$$\mathbf{d}=\frac{0.9\cdot\lambda}{B\cdot\cos\theta} \qquad \mathbf{(3)}$$

where B is the Full Width Half Maximum (FWHM) of the peak of the corresponding crystal plane and λ = 1.5406 Å is the wavelength of X-rays.

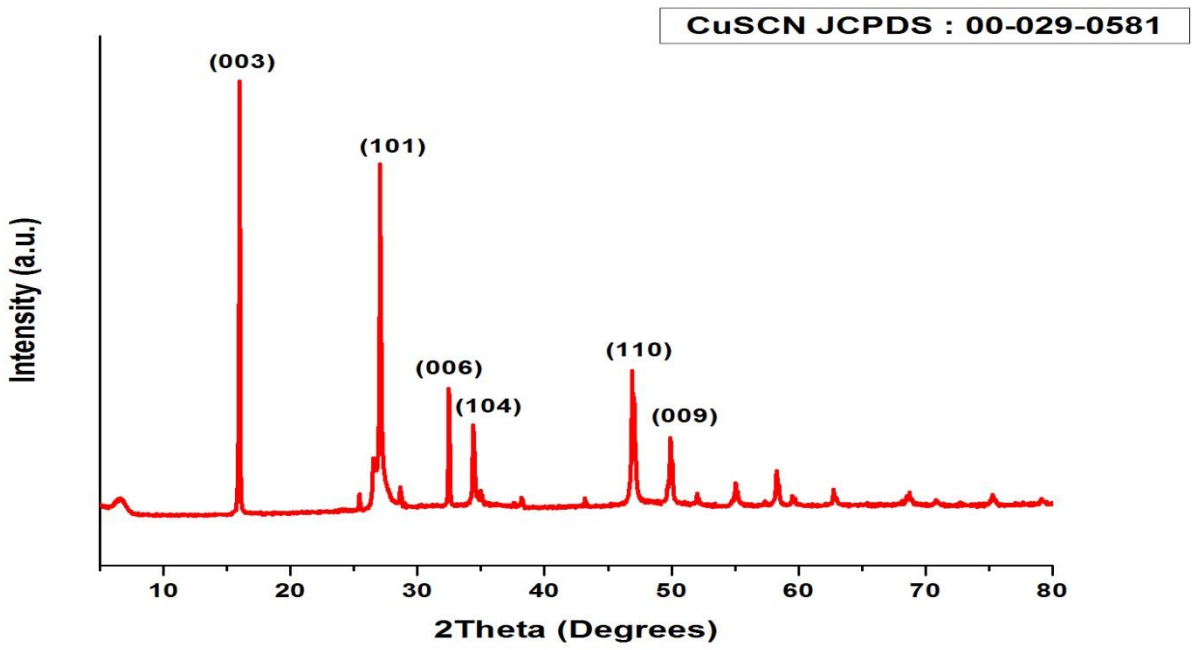

Figure 3.1: XRD spectra of CuSCN powder with the corresponding planes of the β-phase hexagonal crystal structure.

Table 3.1: Diffraction angles and crystallite sizes of the corresponding planes of the hexagonal structured CuSCN

Plane	(003)	(101)	(006)	(104)	(110)	(009)
2θ (º)	15.98	27.04	32.46	34.38	46.93	49.9
Crystallite size (nm)	90.5	49.3	68.9	45.7	28.0	29.7

3.1.2 Optical properties

CuSCN in its powder form has a white-grey color which can be seen also through the absorbance measurements by utilizing the UV-Vis technique. In the optical spectrum (400 nm<wavelength<750 nm) CuSCN powder exhibits low absorbance percentage ranging from 16-10% which explains the white-gray color. Through the absorbance spectrum, by using the Kubelka Mun diagram the band gap of CuSCN can be calculated as Figure 3.2 presents. However, CuSCN's research has not revealed yet its band gap properties, thus both direct and indirect band gap was calculated accordingly. The linear fittings reveal a direct band gap of 3.72 eV and an indirect band gap of 3.48 eV. Both band gaps come in agreement with the respective previous studies [4,5].

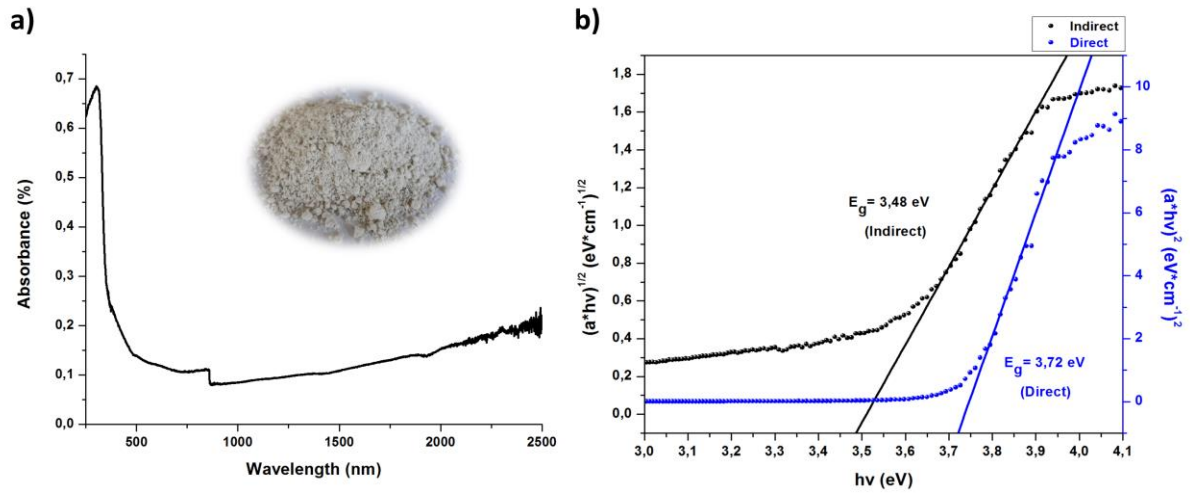

Figure 3.2: a) UV-VIS absorbance spectrum of CuSCN powder, b) Kubelka Munk diagrams for the calculation of the direct and indirect band gap

3.1.3 Morphological Characterization

By utilizing Scanning Electron Microscopy (SEM), the morphology of the pure CuSCN powder was observed and compared with the morphology of the drop casted one. Figure 3.3 reveals that CuSCN powder in its pure form is consisted of crystallites which are agglomerated into bigger grains in order to reduce their surface energy. However when the CuSCN/Methanol solution is sonicated with high sonic frequencies the grains disperse by forming uniform layers of CuSCN crystallites when its drop casted on top of the IDEs. This technique is found to be of great importance while it can develop uniform powder layers with similar thicknesses, which is an important factor when it comes to the gas sensing properties of a sensor.

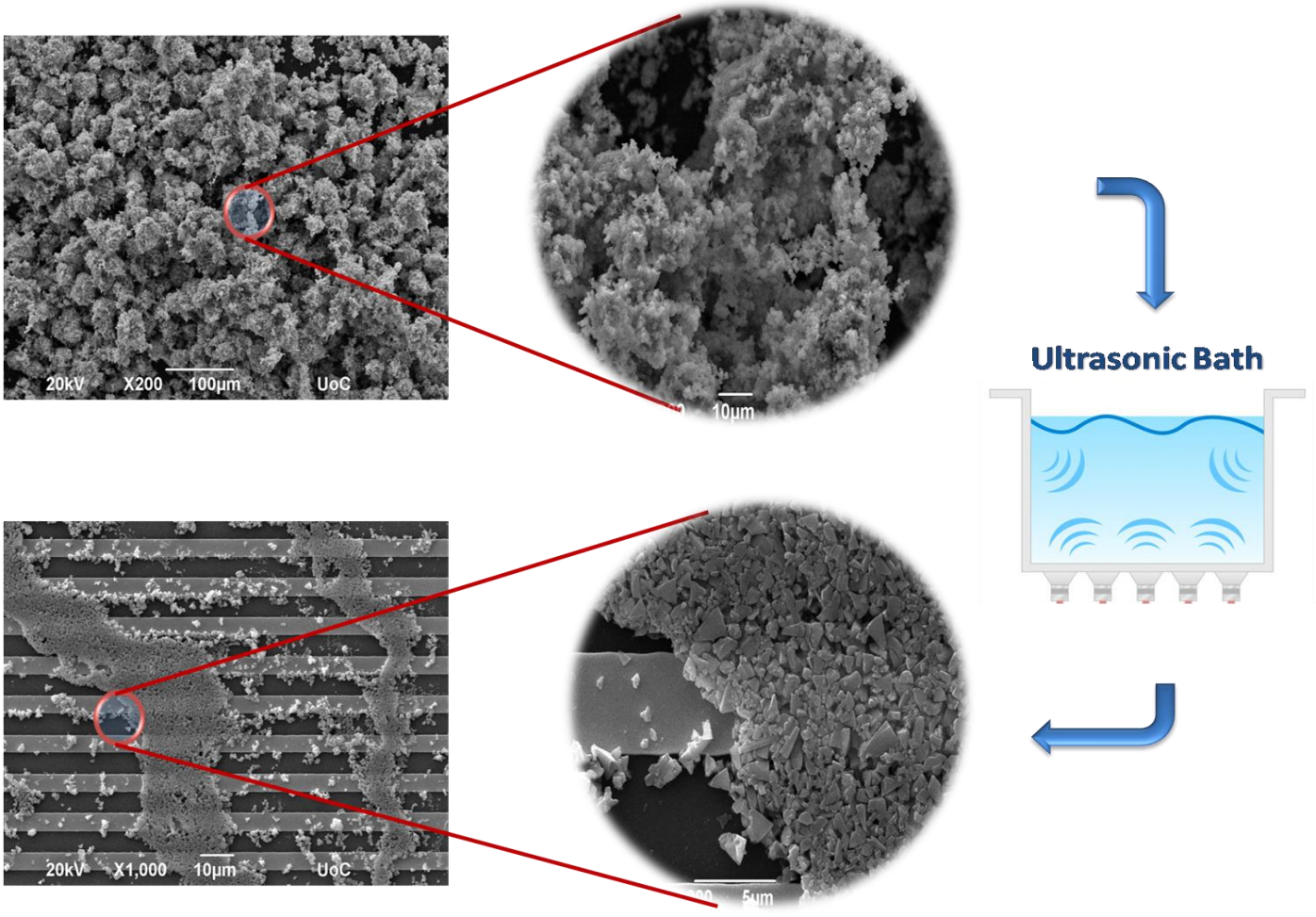

Figure 3.3: SEM pictures of the CuSCN powder before and after the sonication bath procedure.

3.2 Film Characterization

3.2.1 Structural properties

In comparison with CuSCN powder's XRD spectrum, CuSCN/NH_3 and CuSCN/DES films exhibit the same crystal structure with some major differences. As Figure 3.4 reveals, both films exhibit a single crystal plane growth but in different planes. In addition, CuSCN/NH_3 film exhibit high crystallinity while CuSCN/DES exhibit a significantly lower crystallinity which can also be seen through the background noise. By using Scherrer's formula, the crystallite size of each film was calculated and compared with the crystallite size of the respective CuSCN crystal plane. All the results are presented in the Table 3.2 bellow.

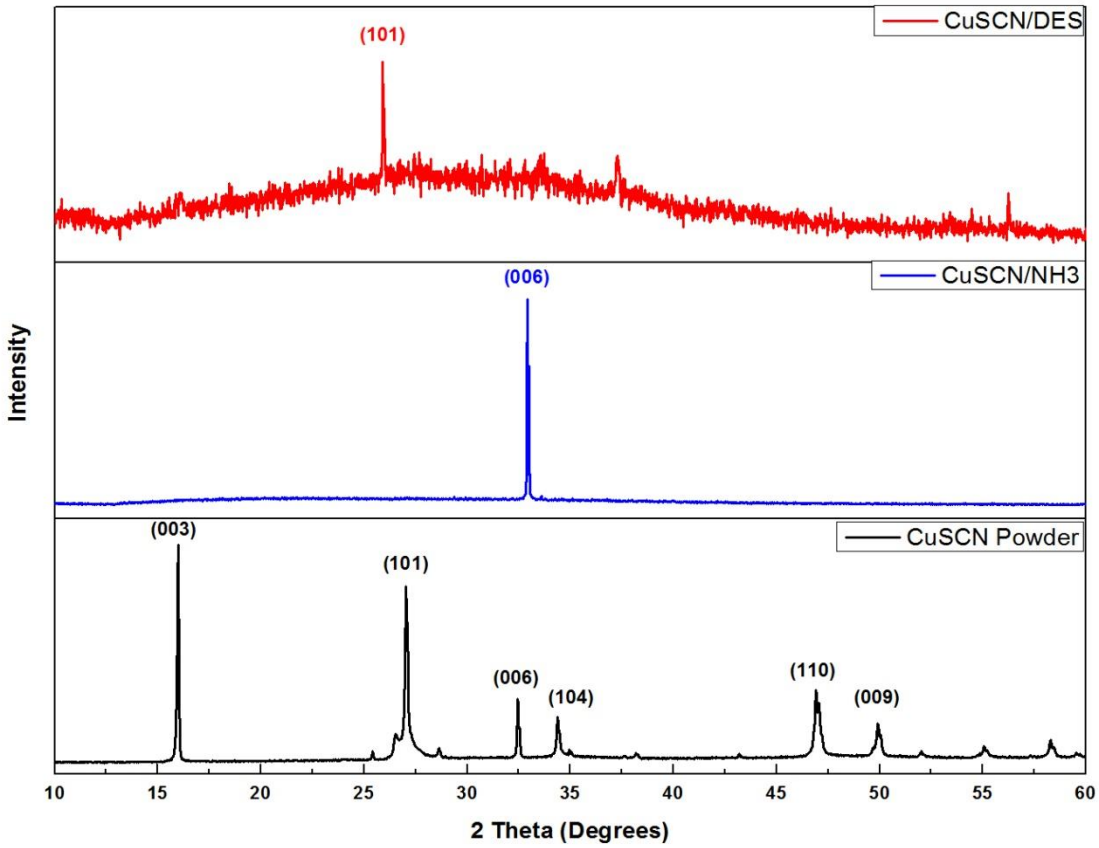

Figure 3.4: XRD spectra of all CuSCN samples.

Table 3.2: Diffraction angles and crystallite sizes of the corresponding planes of all CuSCN samples

Material	Plane	2θ (°)	Crystallite size (nm)
CuSCN Powder	006	32.46	68.9
CuSCN/NH_3	006	32.96	240
CuSCN Powder	101	27.04	49.3
CuSCN/DES	101	25.90	73

The difference in the crystallite size between the powder and the films in their respective planes shows that the CuSCN/NH_3 forms films with a remarkably high crystallinity. This fact can be attributed to the reformation of CuSCN crystals from the Cu^+ and $(SCN)^-$ ions when ammonia is evaporated.

3.2.2 Optical properties

CuSCN films which were deposited on fused silica glasses from both solutions exhibited ultra-high transparency in the complete visible spectrum while it ranges from 80% to 90% as it can be seen in the UV-VIS spectrum in the Figure 3.5 bellow.

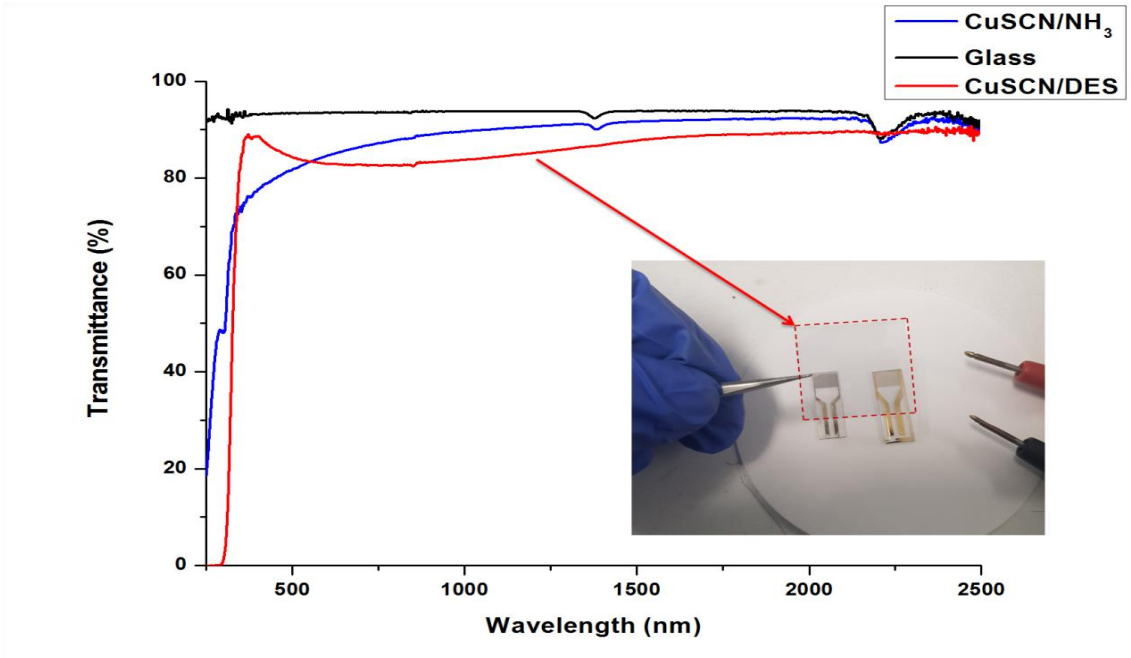

Figure 3.5: Transmittance spectrum of CuSCN/NH_3 and CuSCN/DES films.

These spectrums were also used to calculate the band gaps (direct and indirect) of both films by the Kubelka-Munk technique as Figure 3.6 shows bellow.

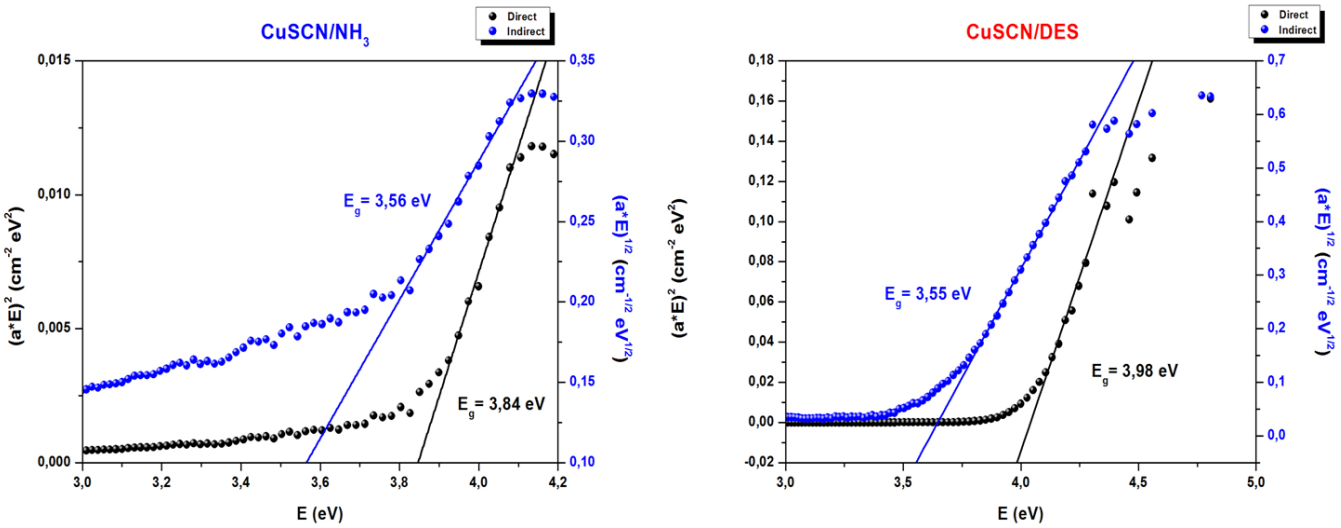

Figure 3.5: Kubelka-Mun diagrams of $CuSCN/NH_3$ and CuSCN/DES films.

Table 3.3: Direct and Indirect band gaps of all CuSCN samples.

Material	Direct Band Gap (eV)	Indirect Band Gap (eV)
CuSCN Powder	3.72	3.48
$CuSCN/NH_3$	3.84	3.56
CuSCN/DES	3.98	3.55

In addition, direct and indirect band gap values for both films were compared with the band gaps of the powder in the Table 3.3. As it can be clearly observed, direct band gap has major differences between all materials, while indirect band gap varies slightly. From this it can be concluded that direct band gap is highly depended from the crystallinity of the material. However, this study is not further explored in this research.

3.2.2 Morphological Characterization

In order to observe the surface of each film in different scales and resolutions, FESEM and Atomic Force Microscopy (AFM) techniques were utilized. In Figure 3.6, FESEM pictures reveal the surface of both films in the same magnification. In both cases, CuSCN films have uniform surface in a large scale, however some major differences can be observed. More specifically, CuSCN/NH_3 films exhibit a smooth surface with the crystallites being well oriented, in contrast with the CuSCN/DES films which seem to have a significant rough and porous surface which is a result of the crystallites agglomeration. This assumption can be heavily supported with the notably higher crystallinity of the CuSCN/NH_3 films as XRD spectra suggested previously.

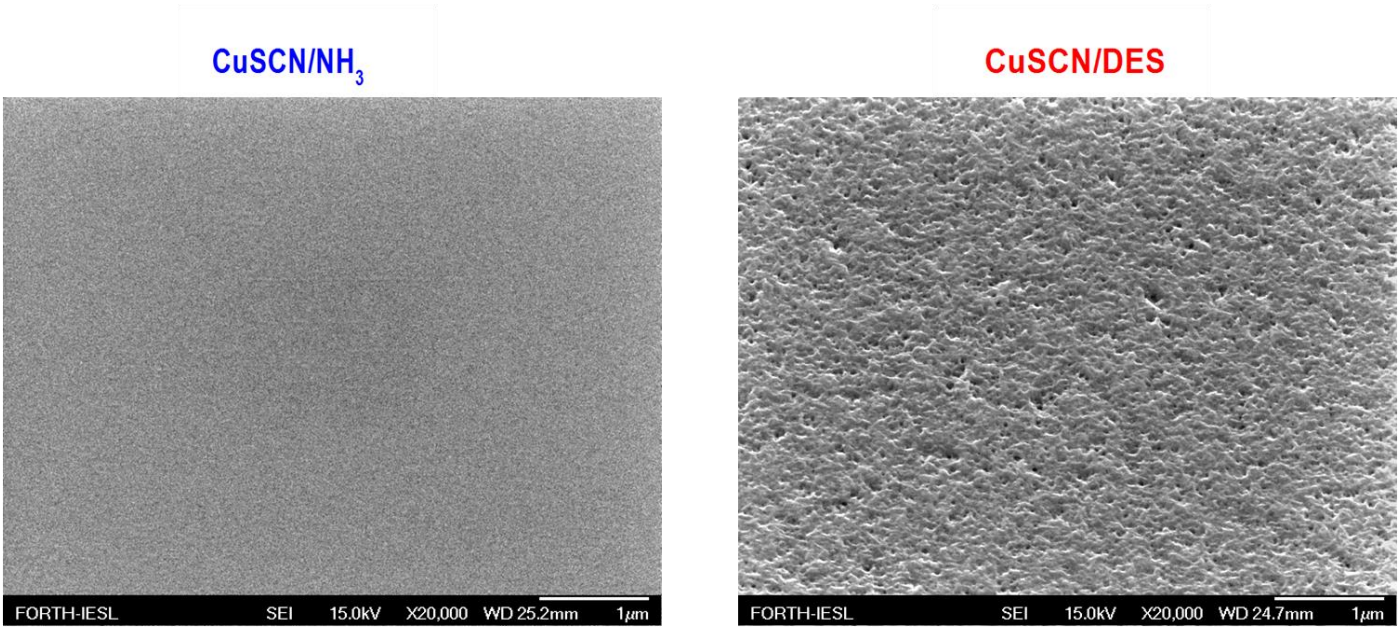

Figure 3.6: FESEM pictures of the CuSCN/NH_3 and CuSCN/DES films' surface.

In pursuance of obtaining pictures with higher resolutions in higher magnification scales, AFM was used for the observation of both films' surface. As Figure 3.6 represents, CuSCN/NH_3 film has remarkably smooth surface with an estimated roughness of 1.8 nm while CuSCN/DES appears to have a considerably higher roughness with a value of 9.7 nm. Furthermore, with the same technique we were able to measure the thickness of both films by creating an incision in the films' area and measure the altitude of the step. The results suggested that CuSCN/NH_3 films appear to be significantly thinner than CuSCN/DES films while the

measured thicknesses were 25 nm and 100 nm respectively. All the data collected from the AFM are provided in the Table 3.4 bellow.

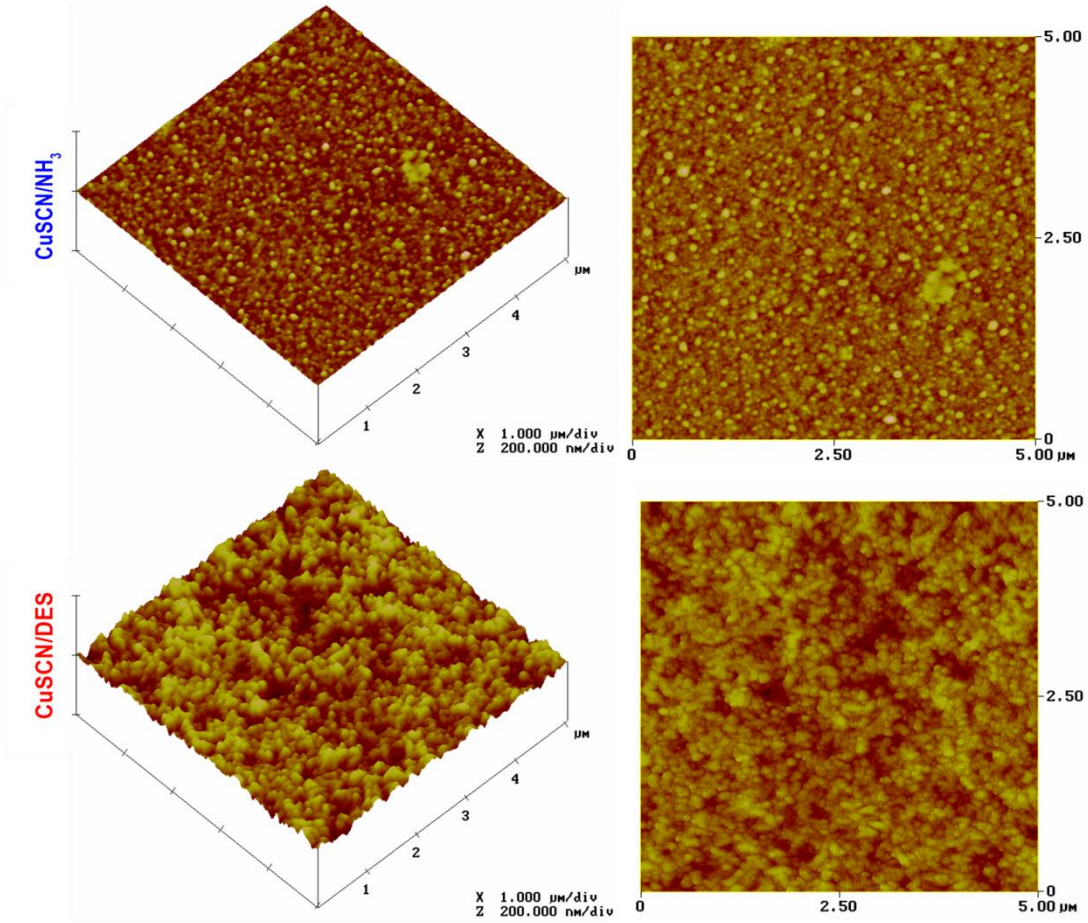

Figure 3.7: AFM 2D and 3D images of the surface of the CuSCN/NH_3 and CuSCN/DES films.

Table 3.4: CuSCN films' roughness and thickness obtained through AFM measurements

Material	Roughness (nm)	Thickness (nm)
CuSCN/NH_3	1.8	25
CuSCN/DES	9.7	100

Chapter 4: Hydrogen Detection

4.1 Gas sensing measurements

As explained previously in Chapter 1, for all the hydrogen sensing measurements the followed procedure was the same. Initially the sensor was placed inside the chamber under vacuum in a pressure of 10^{-3} mbar as to achieve a clean environment for the followed measurements. Shortly after, synthetic air was induced to the chamber with a constant total flow of 500 sccm for 2 hours in order to have a constant current baseline. Afterwards, the synthetic air was mixed with hydrogen gas in the same total flow as to achieve the desired hydrogen concentration and induced inside the chamber for 20 minutes. For the recovery of the sensor the hydrogen supply was ceased for 10 minutes while keeping the total flow steady. The hydrogen concentrations used in all measurements were 1000 ppm, 800 ppm, 600 ppm, 400 ppm and 200 ppm.

4.1.1 CuSCN powder sensing

For a first look of how CuSCN elements are reacting with react oxygen and hydrogen species, CuSCN powder sensors with gold and platinum electrodes were used followed by the procedure mentioned above and with an input voltage of 0.5 Volts.

As Figure 4.1 reveals, CuSCN powder sensors seems to be highly conductive even in the low voltage of 0.5 Volts, which leads to a extremely low power consumption in the range of a 10^{-5} Watts as no further heating source is used. Upon the synthetic air exposure, both sensors increase their conductivity with a slow rate, while a further increase with notably higher rates occur when hydrogen is induced in the chamber. In the case of the Pt electrode sensor, the sensing cycles exhibit a stable and repeatable response while the Au electrode sensor does not work functionally as its not recovers to its initial state. The difference on the recovery as also in the conductivity between the two sensors, cannot be properly explained since the placement of the CuSCN crystallites on the surface of the sensor is random which creates different and paths and thus resistances as a result of the drop casting technique.

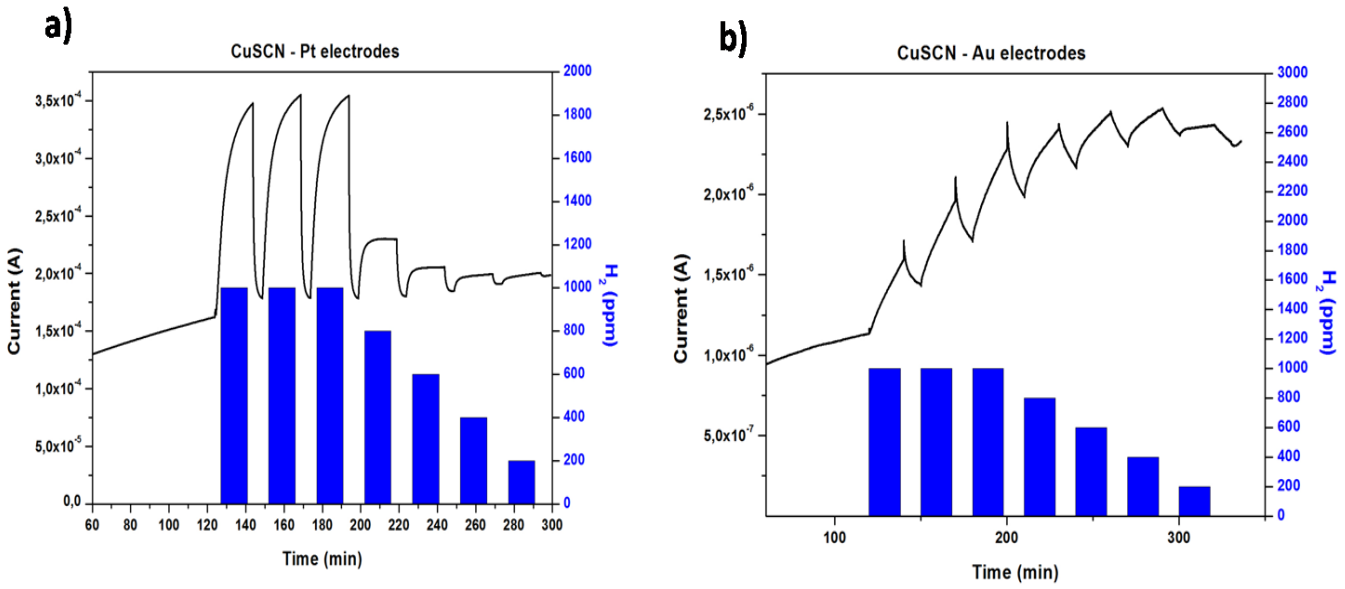

Figure 4.1: Current hydrogen sensing measurements of the CuSCN powder sensors with a) Pt electrodes and b) with Au electrodes.

Nevertheless, a very important observation was that the increase of the conductivity of both sensors in oxygen and hydrogen. Oxygen is widely known oxidizing gas which increases the conductivity of a p-type semiconductor when it is adsorbed on its surface. In comparison with our case, adsorption might fit the description for the oxygen-CuSCN interaction. However, hydrogen in the same scenario is a widely known reductive gas which decreases the conductivity of a p-type semiconductor when it's adsorbed on its surface. This observation can lead to the belief that hydrogen is not adsorbed physically on the surface, with the most possible scenario to be the chemisorption interaction in which hydrogen interacts chemically with the CuSCN's surface and extracts electrons from the conduction band. The sensing mechanism will be further explained in the Chapter 4.2 after all the sensing measurements.

Following the equation (1), the response of the sensor with the platinum electrodes was calculated for all hydrogen concentrations as Figure 4.2 reveals. CuSCN powder exhibits a response of 99.4 % in a concentration of 1000 ppm, while by reducing the concentration inside the chamber the response is reducing as well non-linearly. In the lowest concentration of 200 ppm the response was 5.2 %, suggesting that lower

concentrations might be detected. The response of the sensor with the gold electrodes was not calculated as it is not functioning properly.

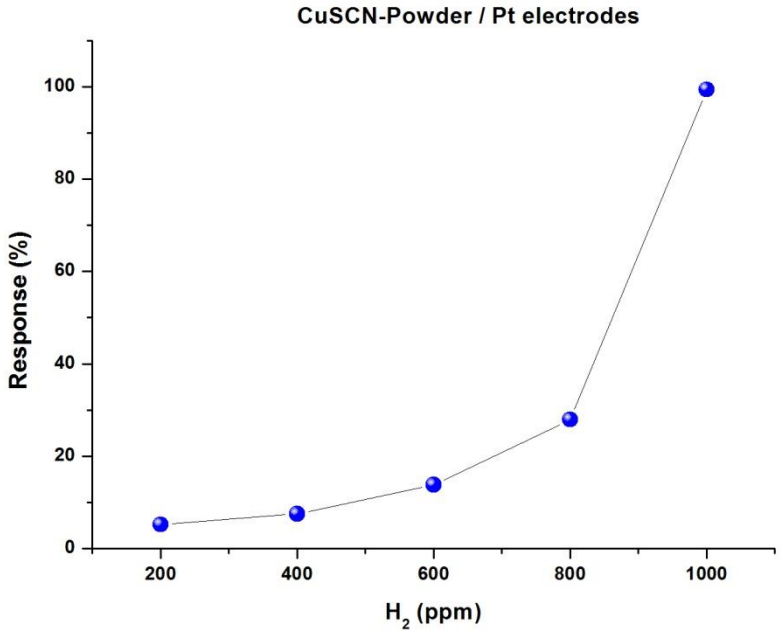

Figure 4.2: Response of the CuSCN powder sensor with platinum electrodes as a function of the corresponding hydrogen concentrations.

In addition, the response and the recovery time of the sensor were investigated. In both cases the corresponding time is calculated based on the time that the sensor needs to reach the 90% of its final current value. Figure 4.3 presents the response time for every hydrogen concentration of the powder sensor with the platinum electrodes. As it can be clearly seen in that case as well the response increases non-linearly with the increase of the concentration, with the calculated time ranging from 654 seconds to 186 seconds. However, the recovery time seems not to be affected by the amount of hydrogen concentration as it has a constant value of 60 seconds in all concentrations, which is considered to be a very short value for a room temperature sensor.

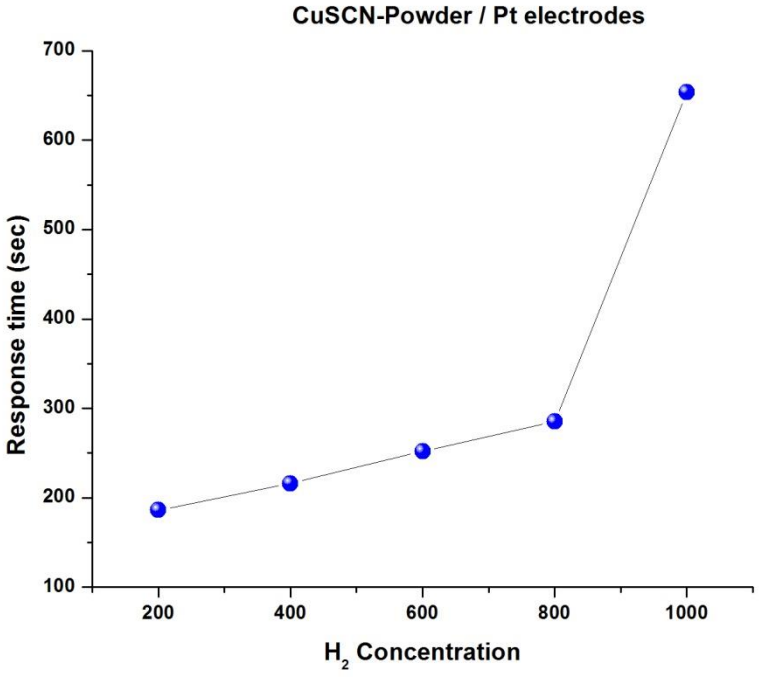

Figure 4.3: The response time of CuSCN powder sensor with platinum electrodes as a function of the hydrogen concentration.

4.1.1 CuSCN thin film sensing

CuSCN powder sensors exhibited some interesting results in the hydrogen detection. However, the repeatability of the drop casting technique can be easily doubted while the pattern of the deposited particles between the electrodes can change dramatically. Thus a more consistent and fundamental study was given on the CuSCN solid films which can be highly more reliable in the matter of the stability of the element deposition.

Following the same procedure with the powder sensors, CuSCN films were tested under the same conditions for hydrogen detection with an input voltage of 0.1 Volts as it was observed that the films were extremely more conductive than the powder. So as for a first step, by keeping the electrodes' distance constant at 5 μm and by using both metals (Au and Pt), the CuSCN films developed from both solutions were compared.

According to the Figure 4.4 bellow, both CuSCN/NH_3 sensors exhibit a similar type of interaction with the powder sensors as not only they increase their conductivity in the presence of hydrogen but also they return

to their initial state when the hydrogen supply cuts off. In addition, it can be observed that the detection for 3 continuous cycles of 1000 ppm remains the same which states that CuSCN/NH_3 sensors exhibit a high stability over the same hydrogen concentrations. However, a major difference in the conductivity of the sensors can be noticed while Pt/CuSCN junctions seem to create a higher resistance than Au/CuSCN junctions as the current magnitude is at the range of 100 μA and 1 mA respectively which also increases the power consumption range of the sensor from 10^{-5} Watts to 10^{-4} Watts. This difference can be attributed to the fact that a very thin layer (~ 1nm) of PtO_2 can exist between the Pt and the CuSCN which is a result of the oxygen plasma treatment. In the case of the Au contacts an oxide layer of Au_2O_3 cannot be formed while it decomposes with the thermal annealing treatment. The decomposing temperature for PtO_2 and Au_2O_3 is at 450°C and 160°C respectively.

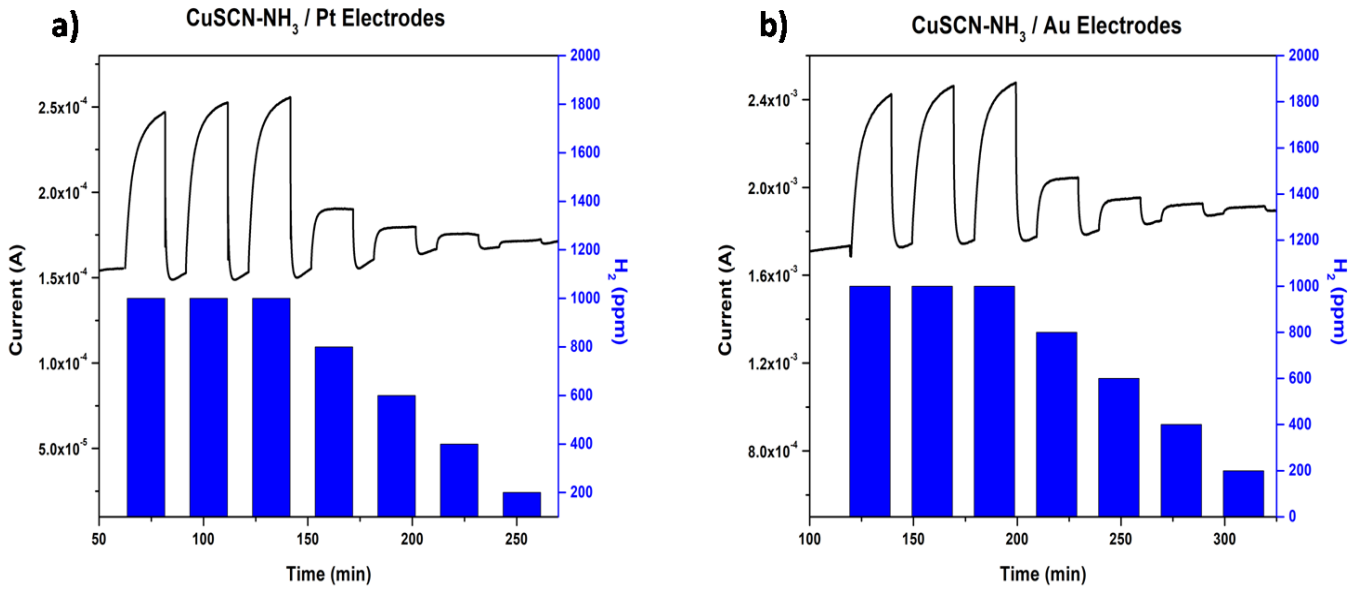

Figure 4.4: Current hydrogen sensing measurements of the CuSCN/NH_3 sensors with, a) Pt electrodes and b) with Au electrodes.

In comparison with CuSCN/NH_3, CuSCN/DES films have some notable differences. As Figure 4.5 reveals, both CuSCN/DES sensors have a similar reaction to hydrogen with the previous sensors with a slight shift in higher currents can be noticed with the pass of time while the sensors do not recover completely. Furthermore, in this case as well the sensor with the Pt electrodes has a higher resistance than the sensor

with the Au electrodes, yet this difference seems to be significantly smaller as the sensors current magnitude is at the range of 100 μA and 300 μA respectively. This observation leads to the belief that CuSCN/DES films have a considerably higher conductivity than the CuSCN/NH_3 films. This assumption can be also supported with the fact that both Pt sensors have quite similar current values although the thickness of the CuSCN/NH_3 is 4 times smaller than CuSCN/DES films, thus higher difference in the current would be expected. The difference in the conductivity between the two films is ought to the fact that CuSCN/NH_3 exhibit a remarkably higher crystallinity than the CuSCN/DES films.

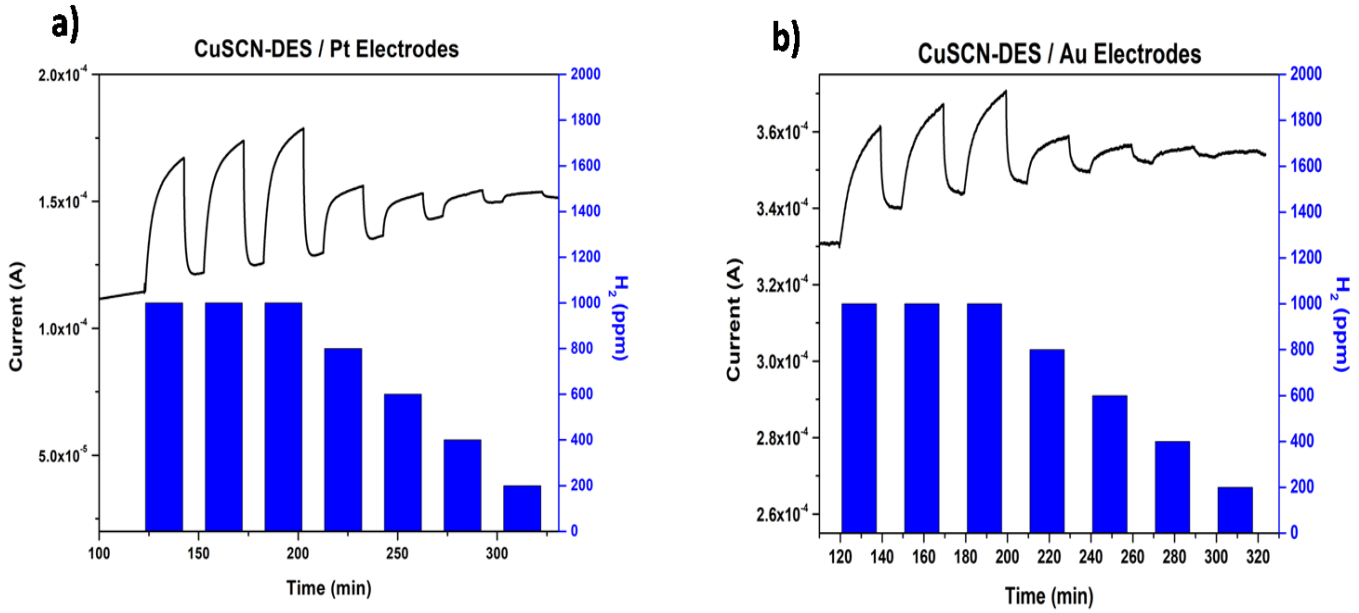

Figure 4.5: Current hydrogen sensing measurements of the CuSCN/DES sensors with, a) Pt electrodes and b) with Au electrodes.

In an effort to compare the efficiency of all the sensors, the response of each sensor was calculated as a function of the hydrogen concentration as it is demonstrated in the Figure 4.6. From the results it can be clearly seen that a similar pattern with the powder sensor occurs as the response increases non-linearly with the increase of the hydrogen concentration for all sensors. Even though the response of all sensors follows a similar pattern, there are some major differences between the electrodes as also between the films.

According to the response diagram, Pt electrodes enhance significantly the response of the sensor in comparison with the Au electrodes for both films, especially in the higher concentrations. This observation

leads to the belief that the high density of electrodes can serve as catalytic areas for the hydrogen since the catalytic behavior of platinum is widely known to be more reacting than gold. Thus, more hydrogen molecules can dissociate into atoms by utilizing Pt electrodes which seems to be chemisorbed in the surface of the CuSCN film and act as acceptors, leading to a further increase of the sensor's conductivity.

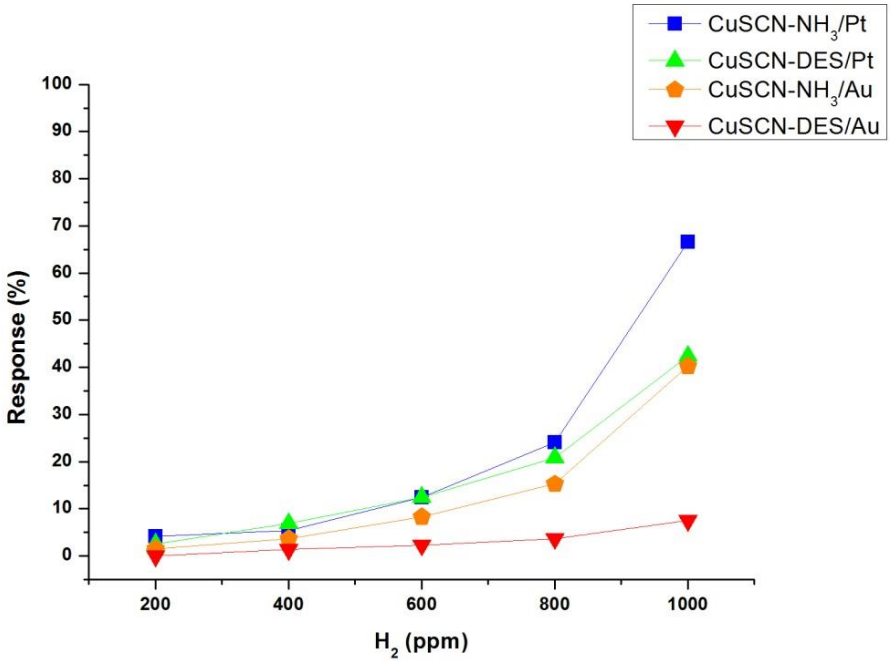

Figure 4.6: Response diagram of all CuSCN film sensors as a function of the hydrogen concentration in room temperature.

As regards to the film preference, it is very clear that films developed by the CuSCN/NH_3 solution exhibit a notably higher response than the films developed by the CuSCN/DES solution when they are compared with the same electrodes. This difference occurs, due to the fact that CuSCN/NH_3 films are remarkably thinner that CuSCN/DES films, resulting to a greater diffusion of the hydrogen molecules and atoms inside the material which leads to a further change of the resistance of the sensor. However, the crystallinity of the material might also play a major role regarding to the sensitivity of CuSCN element, while hydrogen atoms seems to interact in specific positions inside the crystal. This assumption will be further explained in the next chapter.

For all the reasons mentioned above we decide to give an extended focus on the CuSCN/NH_3 sensor as it exhibits the best results for hydrogen sensing measurements. Thus IDEs with palladium electrodes were fabricated in an attempt to further enhance the response of CuSCN/NH_3 films. This idea was based on previous studies [30,31] in which Pd elements found to be a more efficient hydrogen catalyst than Pt elements.

Figure 4.7a reveals the conductometric measurement of the CuSCN/NH_3 film with Pd electrodes towards the same concentrations of hydrogen used in the previous measurements. As it can be seen, the baseline current of the sensor is lower with the respective CuSCN/NH_3 sensors with Pt and Au electrodes while is at range of 30 μA which leads to a further reduce of the power consumption into the range of 3μWatts. However, the current alternation upon the hydrogen exposure in all concentrations seems to increase drastically, which induces a further enhance to the response of the sensor as Figure 4.7b presents, with a remarkably high response value of 179% at 1000 ppm of hydrogen. These results come into agreement with previous prediction that Pd seems to be the best hydrogen catalyst until this time.

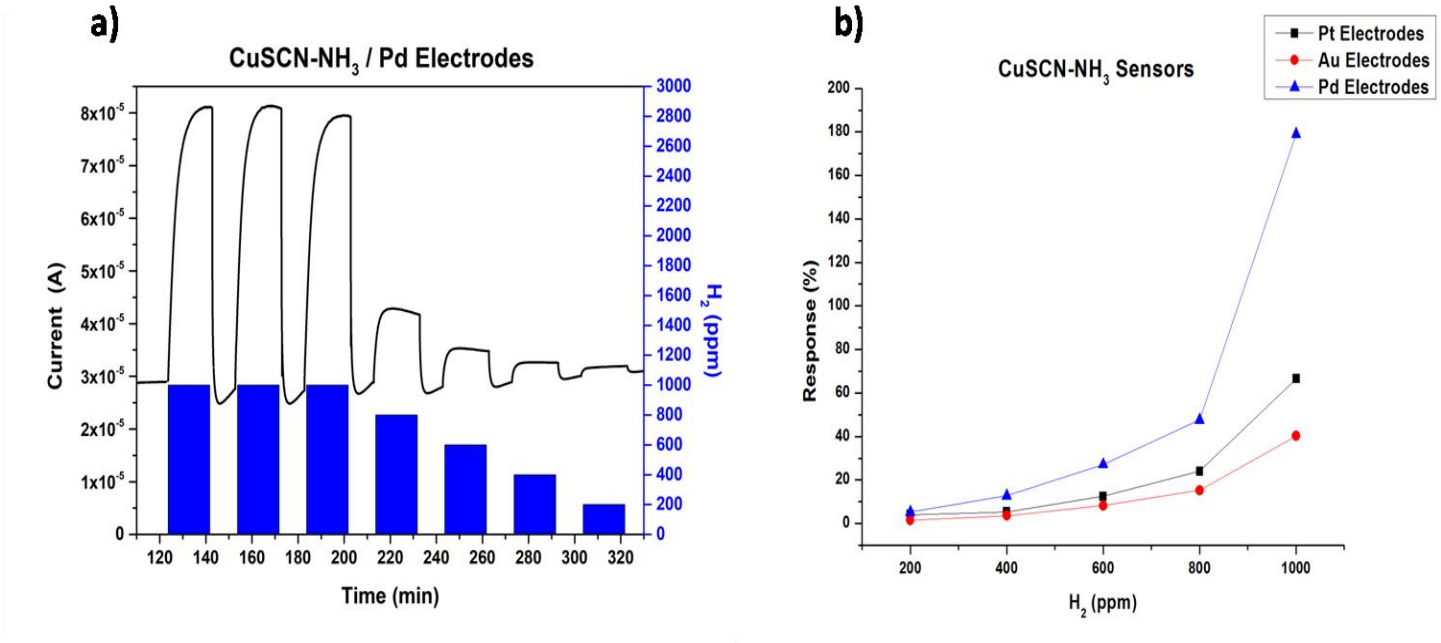

Figure 4.7: a) Current hydrogen sensing measurements of CuSCN/NH_3 sensor with Pd electrodes, b) the response diagram of all CuSCN/NH_3 sensors as a function of the hydrogen concentration.

A further analysis on the CuSCN/NH_3 sensors shows that the response time decreases with the decrease of the hydrogen concentration for all working electrodes, in a similar way with the response, as the Figure 4.8 presents. Thus, low concentrations of hydrogen can be detected rapidly in a room temperature environment. The response time between the sensors with Pd, Pt and Au electrodes differs slightly with the Pt electrodes having a faster reaction to hydrogen compared with the Au electrodes. However, in the case of the Pd electrodes, in high concentrations of hydrogen such as 1000 ppm, the response time is reduces impressively which comes into agreement with the catalytic behavior of the metals. However, equally with the powder sensors, the recovery time remains constant with the change of the concentration with a remarkably rapid value of 60 seconds.

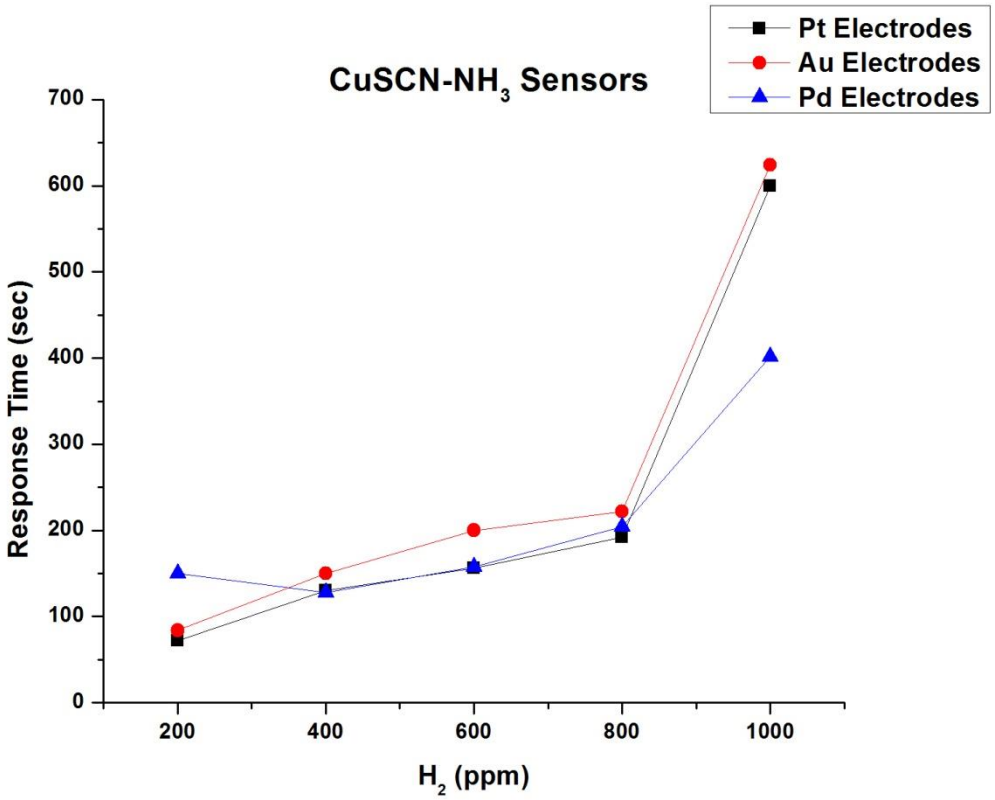

Figure 4.8: The response time of CuSCN/NH_3 sensors with palladium, platinum and gold electrodes as a function of the hydrogen concentration.

Additionally, in an effort to observe the change of the resistance of the CuSCN/NH_3 sensors, current values were measured as a function of the input voltage (I-V measurements) in the presence of vacuum, synthetic air and 1000 ppm of hydrogen in that order. The range of the input voltage was limited from -0.1 Volts to

0.1 Volts as a precaution of destroying the sensor or the multimeter through extremely high current flows. As Figure 4.9 indicates, both sensors reveal a perfectly linear behavior in all environments suggesting that the resistance remains constant in this range of input voltages, thus even lower voltages than 0.1 Volts can be used for hydrogen detection. The difference in the resistance through the change of the environment can be clearly seen for each sensor similarly, as in the presence of vacuum both sensors exhibit their lowest conductivity, followed by a higher conductivity in the presence of synthetic air and the highest conductivity in the presence of 1000 ppm of hydrogen. The difference in the hydrogen detection between the Pd, Pt and Au electrodes can be also noticed, as explained previously, as Pd electrodes seems to drift the response of the sensor in much higher values. By using a linear fitting, the resistance of each sensor was calculated in all environments respectively and presented in the Table 4.1 bellow in order to observe the change of resistance as well.

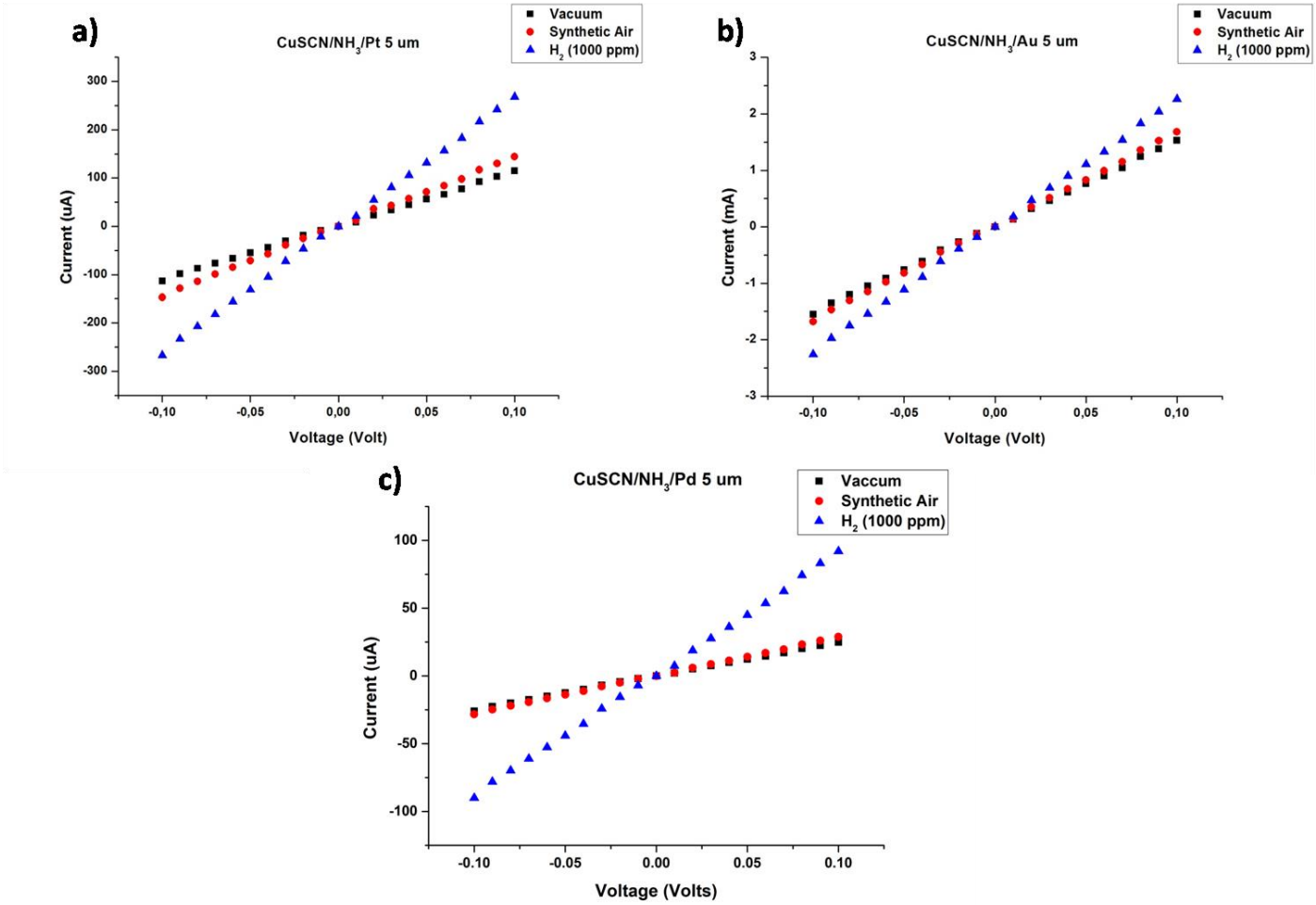

Figure 4.9: I-V measurements of $CuSCN/NH_3$ sensors with a) platinum, b) gold and c) palladium electrodes in the presence of vacuum, synthetic air and 1000 ppm of hydrogen

Table 4.1: Resistance values of the $CuSCN/NH_3$ sensors with Pt, Au and Pd electrodes in the presence of vacuum, synthetic air and 1000 ppm of hydrogen

Sensor	R_{vacuum} (Ohm)	R_{air} (Ohm)	R_{gas}(Ohm)
$CuSCN/NH_3$-Pd	3992.0	3548.6	1116.6
$CuSCN/NH_3$-Pt	896.9	698.3	379.2
$CuSCN/NH_3$-Au	65.9	60.2	44.8

.

4.2 Gas sensing mechanism

As explained in Chapter 1, in a simple model of the interaction between oxygen molecules and metal oxides, oxygen species create weak Wan der Waals bonds with the surface of the metal oxide as O_2^- (<100 ^oC), O^- (100–300 ^oC) and O^{2-} (>300 ^oC) in the vicinity of defects which are caused by oxygen vacancies, while they abstract electrons from the valence band, leading into an increase of the hole concentration. Thereby, oxygen adsorption in the surface of a p-type metal oxide will increase its conductivity. On the other hand, when hydrogen molecules are induced inside the chamber, they interact with absorbed oxygen species by forming water molecules which are released back into the chamber. This procedure will return the abstracted electrons back to the semiconductor, therefore the hole concentration is reduced which means that in the case of a p-type metal oxide, the conductivity will be decreased. However, there is no known study on how oxygen and hydrogen species interact with thiocyanate based semiconductors such as CuSCN.

In a previous study, Tsetseris [2] focused on the defects and the impurities inside of the crystal structure of CuSCN, by utilizing Density Functional Theory (DFT) calculations. In these calculations, copper (Cu) and thiocyanate (SCN) vacancies were used to observe changes in the density of states (DOS) of CuSCN supercells. As Figure 4.10 reveals, Cu vacancies are dominant by creating states inside the valence band and by shifting the Fermi level (fixed at 0 eV) bellow the valence band maximum which explains their role in the p-type characteristics of CuSCN. On the contrary, SCN vacancies seem to create small states bellow conduction band which contribute to the increase of the electron concentration.

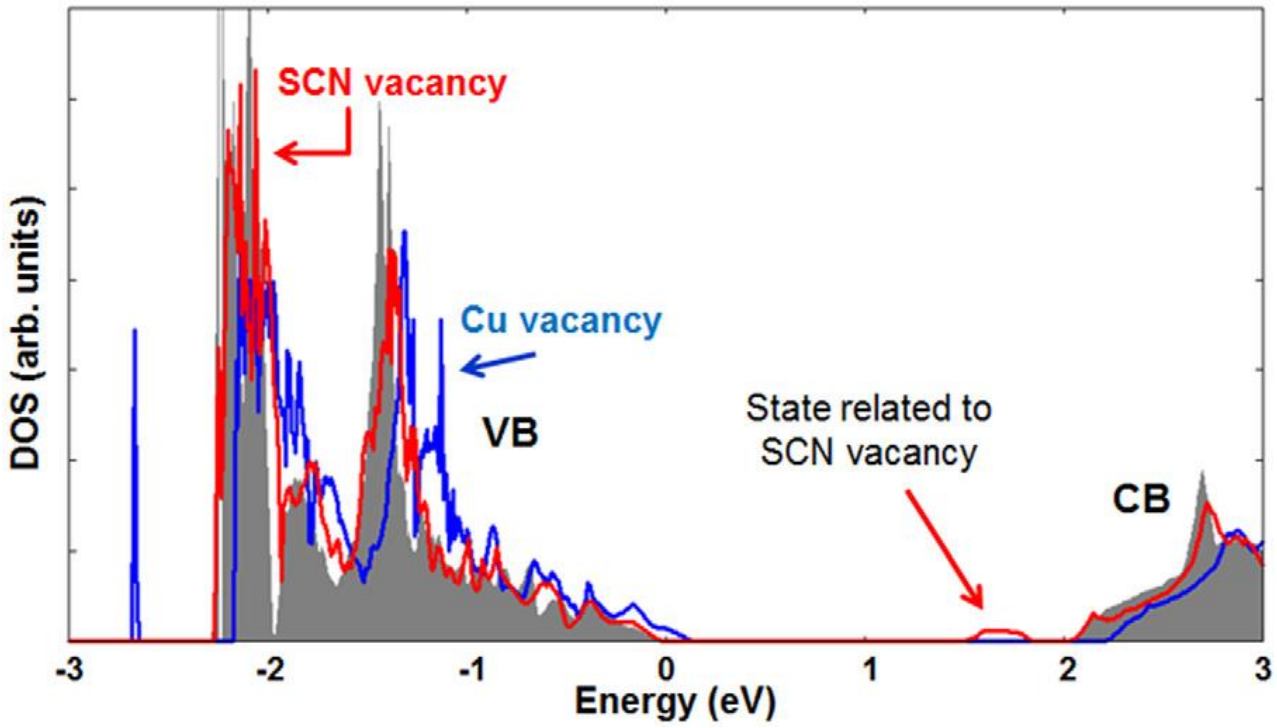

Figure 4.10: Electronic densities of states of *β*-CuSCN with no defects (shaded area) and of *β*-CuSCN with a Cu vacancy (blue line) or a SCN vacancy (red line). Zero of energy is set at the Fermi level.

In this work, professor Tsetseris contributed with similar DFT calculations based on the conductometric measurements of all sensors. In specific, by employing calculation of large supercells of the β phase of CuSCN with 24 chemical units in the pristine case, the interaction between CuSCN, oxygen and hydrogen species was studied.

The results on the oxidation of the surface due to the presence of oxygen molecules, revealed two different configurations as Figure 4.11 reveals. In the first configuration an oxygen molecule is physisorbed in the vicinity of a Cu atom with weak Van der Waals forces and a binding energy of 36 meV. This physisorption leads to the creation of shallow states inside the band gap close to the valence band maximum which results to an increase of the p-type conductivity as the DOS diagram in Figure 4.11c suggests. However, the second configuration seems to be more stable, while oxygen molecules decompose into oxygen atoms and are chemisorbed on the CuSCN surface by creating strong covalent bonds with carbon atoms with a binding energy of 1.636 eV. The chemisorbed oxygen atoms will also induce an increase of the p-type conductivity while they create states right next to the valence band maximum.

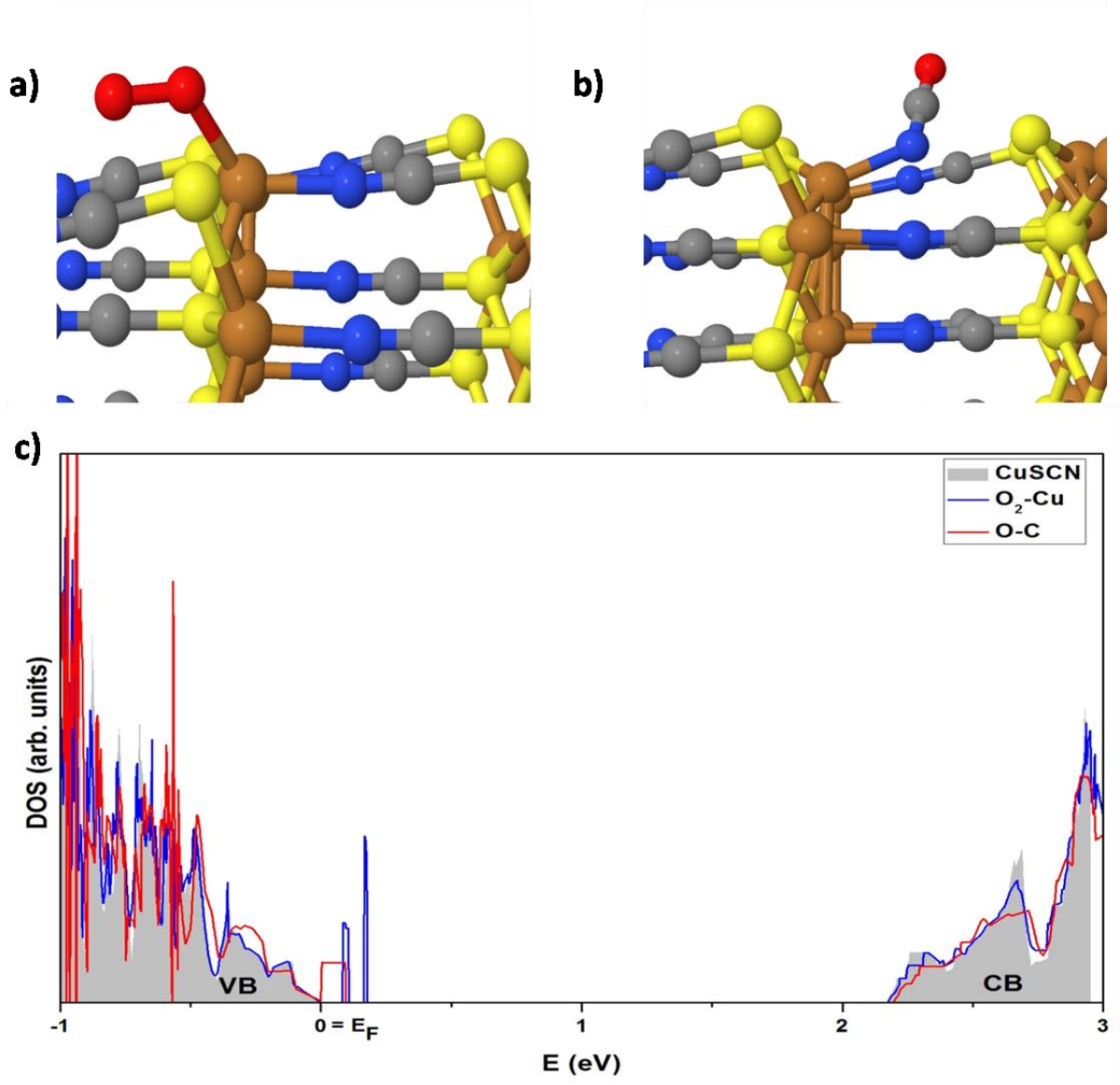

Figure 4.11: Configuration of a) a physisorped oxygen molecule, b) a chemisorped oxygen atom (Cu: brown, S: yellow, C: gray, N: blue, O: red spheres) and c) the corresponding DOS compared to the pristine CuSCN. Zero of energy is set at the Fermi level.

In the case of the interaction between hydrogen species and the surface of CuSCN two more configurations was found as presented in Figure 12. Both configurations are based on the chemisorption of hydrogen atoms since hydrogen molecules did not seem to interact with the pristine CuSCN neither physically nor chemically. The first configuration suggests that a hydrogen atom creates a covalent bond with carbon atom with a bonding energy of 0.68 eV while the second configuration suggests that two hydrogen atoms found in the vicinity of a Cu defect will create covalent bonds with the carbon and the nitrogen atoms with a bonding

energy of 1.02 eV. Both complexes found to shift the Fermi level inside the valence band as the DOS diagram reveals, which results to an increase of the p-type conductivity.

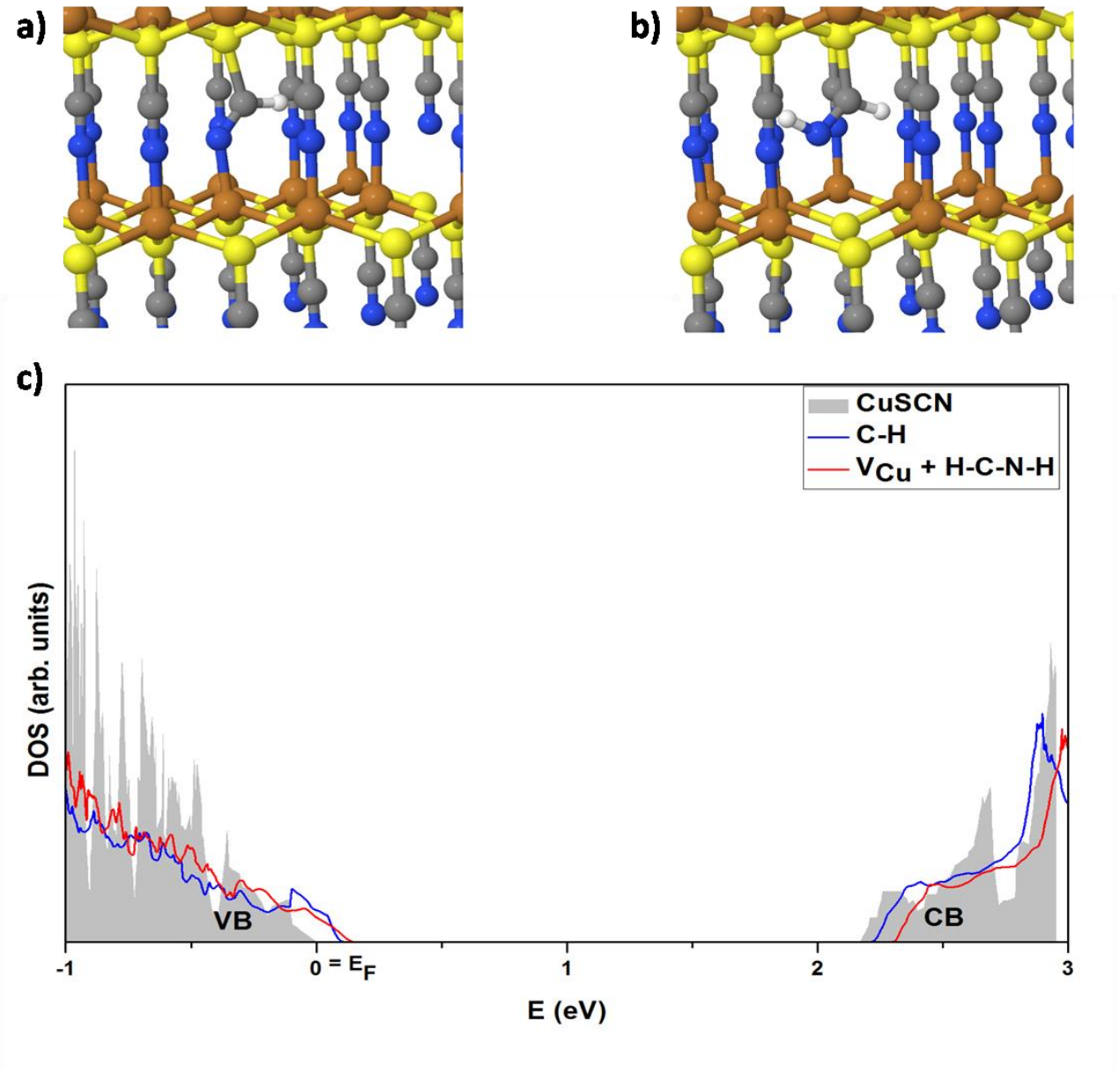

Figure 4.12: Configuration of a) a single chemisorbed hydrogen atom, b) a pair of chemisorped hydrogen atom (Cu: brown, S: yellow, C: gray, N: blue, H: hydrogen spheres) and c) the corresponding DOS compared to the pristine CuSCN. Zero of energy is set at the Fermi level.

In addition, the case of interaction of hydrogen atoms in the already oxidized surface of CuSCN was studied. The results which are presented in the Figure 4.13 revealed two more stable configurations. In the first configuration a hydrogen atom creates a covalent bond with the sulfur atom while in the second one, it creates a similar bond with nitrogen atom. The configuration shown in Figure 4.13a is more stable than that

in Figure 4.13b by 0.10 eV and more stable than an ejected isocyanic acid by 0.55 eV. In both cases, the p-type conductivity is further increased while they both form shallow states inside the band gap close to the valence band maximum as the DOS diagram reveals.

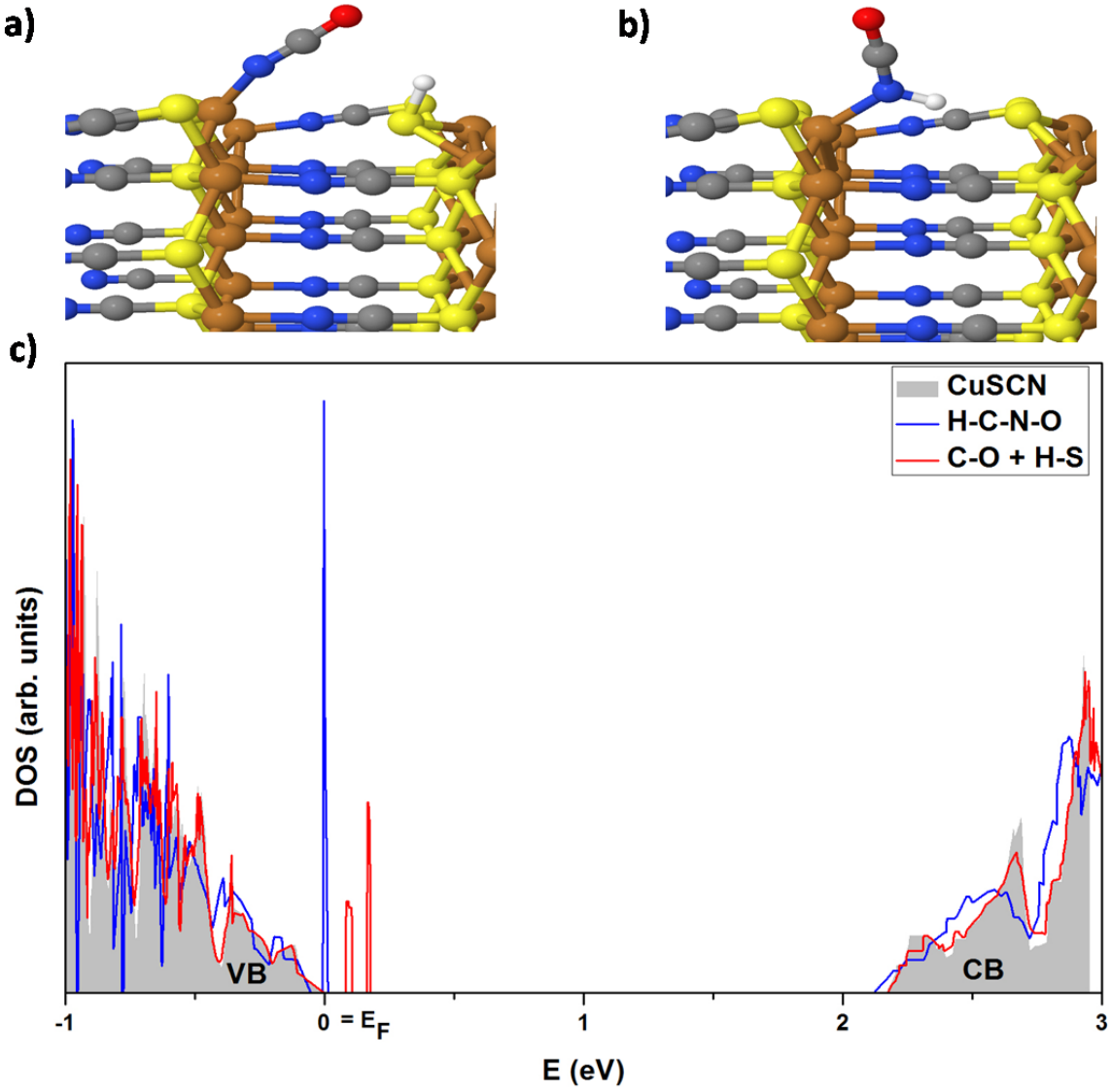

Figure 4.13: Oxygen and hydrogen complexes on the CuSCN surface with the formation of a) a single O-C-N-H bond, b) a C-O bond and S-H bond (Cu: brown, S: yellow, C: gray, N: blue, H: hydrogen spheres) and c) the corresponding DOS compared to the pristine CuSCN. Zero of energy is set at the Fermi level.

All these calculations are of great importance while they explain the big differences between the responses of all sensors with the different electrodes. Since molecular hydrogen seems not to interact with the surface of CuSCN, hydrogen catalysts have to play a significant role on these interactions. Our results comes into

agreement with the theory which indicates that palladium is the best catalyst for hydrogen in a room temperature as also that platinum is more reactive than gold.

Regarding to the recovery mechanism, in all configurations, hydrogen seems to be released back to the chamber with a simple chemical desorption mechanism. Chemical desorption is a phenomenon whereby a substance is released from or through a surface. The process is the opposite of chemisorption. This occurs in a system being in the state of chemisorption equilibrium between a gas solution and an adsorbing surface. When the concentration (or pressure) of substance in the bulk phase is lowered, some of the chemisorbed substance is released back to the environment. Thus in our case, when the hydrogen supply cuts of, the chemisorbed hydrogen atoms are released from the surface and forms water molecules with the oxygen species of the synthetic air.

According to the hydrogen sensing mechanism, the difference between the response of CuSCN/NH_3 and CuSCN/DES films can be explained. The greater thickness of CuSCN/DES impacts on the interaction between the hydrogen atoms and the CuSCN layers which are located close to the substrate, as the hydrogen atoms are unable to diffuse so deep inside the material. Thus only the layers close to the surface will alter their resistivity which will lead to a smaller modification of the total current. In addition to that, the superior crystallinity of the CuSCN/NH_3 films may also affect the interface, as hydrogen atoms will interact properly with the plausible mechanisms mentioned above only inside the vicinity of a well oriented crystallite.

Chapter 5: Discussion

CuSCN nanostructures seem to be an excellent choice for sensing elements for hydrogen detection while they reveal high responses towards low concentrations of hydrogen with a room working temperature and an extremely low bias input. In this work, the best results found to be on CuSCN thin films processed by aqueous ammonia alongside with the Pd electrodes.

Based on an extended literature review [19,24,32–36], the CuSCN sensor mentioned above was compared to the best hydrogen sensing elements that are publicized, in a 3D diagram as Figure 5.1 presents. These are the most reliable hydrogen sensors with a room working temperature, while they exhibit a full recovery after the exposure of different concentrations of hydrogen gas, with no background noise. Therefore, the stability of the sensors can be clearly seen through the stable sensing cycles in all cases. The diagram bellow reveals that CuSCN has the best response towards 1000 ppm of hydrogen with the lowest input voltage. In addition the increased input voltage of these sensors can lead to a further increase of the power consumption due to the self-heating effect. In our case the extremely low input voltage keeps the actual power consumption into low levels.

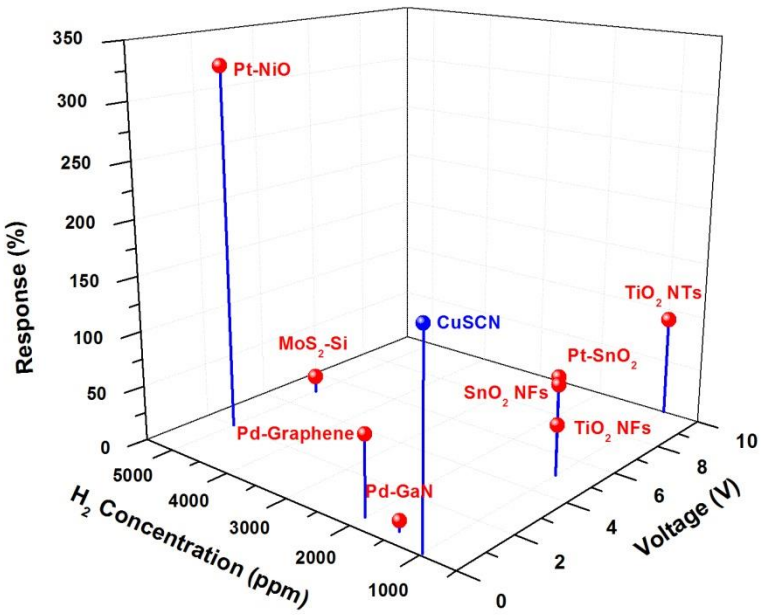

Figure 5.1: 3D response diagram of the best hydrogen sensors found on the literature with a room working temperature as a function of the hydrogen concentration and the input voltage.

Chapter 6: Conclusion

In this work, the novel material CuSCN was studied extendedly as a potential candidate for low cost hydrogen sensors. By using solution based methods, different types of CuSCN nanostructures were developed such as dispersed powder and thin solid films. These structures were deposited on top of silicon wafers and fused silica glasses in order to analyze their optical, structural and morphological properties. The results showed that all samples exhibit a β-phase CuSCN crystal structure with different planes of growth which was depended from the synthesis of the solution, while also they exhibit a wide band gap in the range of 3.48 eV- 3.98 eV which leads to highly transparent films. Regarding of the films, ammonia (NH_3) found to be an excellent solvent while it forms extremely smooth and thin films (25nm) with a high crystallinity in comparison with the diethyl sulfide (DES) which forms notably thicker and rougher films with a significantly lower crystallinity.

Towards the gas sensing properties, all samples were deposited on top of homemade gold and platinum interdigitated electrodes (IDEs) and tested upon low concentrations of hydrogen in a room temperature with an extremely low voltage input (0.5 Volts for the powder sensors and 0.1 Volts for the film sensors). All sensors found to have an impressively high conductivity while they could detect low concentrations of hydrogen rapidly, with a unique mechanism without a noisy background. All sensors exhibited a fast recovery time of 60 seconds.

By comparing the sensors it was revealed that the high density of the noble metal electrodes can work as catalytic areas for the hydrogen molecules which decompose them into atoms and diffuse them inside the CuSCN crystallites, wherein hydrogen atoms are chemisorbed on the surface, which will further increase the p-type conductivity. Thus, the palladium electrodes were considered as more functional while they have better catalytic properties than platinum and gold electrodes.

Moreover, CuSCN films developed by NH_3 solvent found to be the best candidate as a hydrogen sensor while their deposition is highly repeatable in comparison with the powder sensors. Furthermore, the thinner profile with the higher crystallinity of the CuSCN/NH_3 films was observed to enhance the interaction with the hydrogen species.

Summing up, this work is of great importance while it proves that CuSCN nanostructures are a possible solution for low cost and low power hydrogen sensors in the industrial section. The high conductivity and stability of the sensors with the low working temperature reduces the power consumption into the range of μWatts which suggests that they can be used in microelectromechanical systems (MEMS) and chips with a voltage input of a small battery.

References

[1] Smith D L and Saunders V I 1982 Preparation and structure refinement of the 2H polytype of β-copper(I) thiocyanate *Acta Crystallogr. Sect. B Struct. Crystallogr. Cryst. Chem.*

[2] Tsetseris L 2016 Copper thiocyanate: Polytypes, defects, impurities, and surfaces *J. Phys. Condens. Matter*

[3] Tsetseris L 2016 Two-dimensional copper thio- and seleno-cyanates *Phys. Chem. Chem. Phys.*

[4] Pattanasattayavong P, Promarak V and Anthopoulos T D 2017 Electronic Properties of Copper(I) Thiocyanate (CuSCN) *Adv. Electron. Mater.*

[5] Pattanasattayavong P, Mottram A D, Yan F and Anthopoulos T D 2015 Study of the Hole Transport Processes in Solution-Processed Layers of the Wide Bandgap Semiconductor Copper(I) Thiocyanate (CuSCN) *Adv. Funct. Mater.*

[6] Ji H, Zeng W and Li Y 2019 Gas sensing mechanisms of metal oxide semiconductors: A focus review *Nanoscale*

[7] Feng P, Shao F, Shi Y and Wan Q 2014 Gas sensors based on semiconducting nanowire field-effect transistors *Sensors (Basel).*

[8] Ramgir N S, Sharma P K, Datta N, Kaur M, Debnath A K, Aswal D K and Gupta S K 2013 Room temperature H2S sensor based on Au modified ZnO nanowires *Sensors Actuators, B Chem.*

[9] Aricò A S, Bruce P, Scrosati B, Tarascon J M and Van Schalkwijk W 2005 Nanostructured materials for advanced energy conversion and storage devices *Nat. Mater.*

[10] Cheng L, Chen Q, Li J and Liu H 2020 Boosting the photocatalytic activity of CdLa2S4 for hydrogen production using Ti3C2 MXene as a co-catalyst *Appl. Catal. B Environ.*

[11] Wu G, More K L, Johnston C M and Zelenay P 2011 High-performance electrocatalysts for oxygen

reduction derived from polyaniline, iron, and cobalt *Science (80-.).*

[12] Jiao Y, Zheng Y, Jaroniec M and Qiao S Z 2015 Design of electrocatalysts for oxygen- and hydrogen-involving energy conversion reactions *Chem. Soc. Rev.*

[13] Basnet A and Zhong J 2020 Integrating gas energy storage system in a peer-to-peer community energy market for enhanced operation *Int. J. Electr. Power Energy Syst.*

[14] Schlapbach L and Züttel A 2001 Hydrogen-storage materials for mobile applications *Nature*

[15] Wagner F T, Lakshmanan B and Mathias M F 2010 Electrochemistry and the future of the automobile *J. Phys. Chem. Lett.*

[16] Eberle U, Müller B and Von Helmolt R 2012 Fuel cell electric vehicles and hydrogen infrastructure: Status 2012 *Energy Environ. Sci.*

[17] Crowl D A and Jo Y Do 2007 The hazards and risks of hydrogen *J. Loss Prev. Process Ind.*

[18] Kim J H, Mirzaei A, Kim H W and Kim S S 2019 Improving the hydrogen sensing properties of SnO2 nanowire-based conductometric sensors by Pd-decoration *Sensors Actuators, B Chem.*

[19] Chen Z, Hu K, Yang P, Fu X, Wang Z, Yang S, Xiong J, Zhang X, Hu Y and Gu H 2019 Hydrogen sensors based on Pt-decorated SnO2 nanorods with fast and sensitive room-temperature sensing performance *J. Alloys Compd.*

[20] Vallejos S, Gràcia I, Pizúrová N, Figueras E, Čechal J, Hubálek J and Cané C 2019 Gas sensitive ZnO structures with reduced humidity-interference *Sensors Actuators, B Chem.*

[21] Lupan O, Postica V, Labat F, Ciofini I, Pauporté T and Adelung R 2018 Ultra-sensitive and selective hydrogen nanosensor with fast response at room temperature based on a single Pd/ZnO nanowire *Sensors Actuators, B Chem.*

[22] Zhou X, Wang Z, Xia X, Shao G, Homewood K and Gao Y 2018 Synergistic Cooperation of Rutile TiO2 {002}, {101}, and {110} Facets for Hydrogen Sensing *ACS Appl. Mater. Interfaces*

[23] Nakate U T, Lee G H, Ahmad R, Patil P, Hahn Y B, Yu Y T and Suh E kyung 2018 Nano-bitter

gourd like structured CuO for enhanced hydrogen gas sensor application *Int. J. Hydrogen Energy*

[24] Wu C H, Zhu Z, Chang H M, Jiang Z X, Hsieh C Y and Wu R J 2020 Pt@NiO core–shell nanostructure for a hydrogen gas sensor *J. Alloys Compd.*

[25] Walewyns T, Spirito D and Francis L A 2014 A tunable palladium-based capacitive MEMS hydrogen sensor performing high dynamics, high selectivity and ultra-low power sensing *Procedia Engineering*

[26] Guan D, Yang F, Liu Q, Yu K and Sun J 2017 A novel prototype of low power consumption MEMS sensors for hydrogen detection *Proceedings of IEEE Sensors*

[27] Hübert T, Boon-Brett L, Black G and Banach U 2011 Hydrogen sensors - A review *Sensors Actuators, B Chem.*

[28] Striccoli M 2017 Photolithography based on nanocrystals *Science (80-.).*

[29] Chaudhary N, Chaudhary R, Kesari J P and Patra A 2017 An eco-friendly and inexpensive solvent for solution processable CuSCN as a hole transporting layer in organic solar cells *Opt. Mater. (Amst).*

[30] Singh S A, Vishwanath K and Madras G 2017 Role of Hydrogen and Oxygen Activation over Pt and Pd-Doped Composites for Catalytic Hydrogen Combustion *ACS Appl. Mater. Interfaces*

[31] Morfin F, Sabroux J C and Renouprez A 2004 Catalytic combustion of hydrogen for mitigating hydrogen risk in case of a severe accident in a nuclear power plant: Study of catalysts poisoning in a representative atmosphere *Appl. Catal. B Environ.*

[32] Liu G, Wang Z, Chen Z, Yang S, Fu X, Huang R, Li X, Xiong J, Hu Y and Gu H 2018 Remarkably enhanced room-temperature hydrogen sensing of SnO2 nanoflowers via vacuum annealing treatment *Sensors (Switzerland)*

[33] Johnson J L, Behnam A, Pearton S J and Ural A 2010 Hydrogen sensing using Pd-functionalized multi-layer graphene nanoribbon networks *Adv. Mater.*

[34] Enachi M, Lupan O, Braniste T, Sarua A, Chow L, Mishra Y K, Gedamu D, Adelung R and

Tiginyanu I 2015 Integration of individual TiO2 nanotube on the chip: Nanodevice for hydrogen sensing *Phys. Status Solidi - Rapid Res. Lett.*

[35] Lim W, Wright J S, Gila B P, Johnson J L, Ural A, Anderson T, Ren F and Pearton S J 2008 Room temperature hydrogen detection using Pd-coated GaN nanowires *Appl. Phys. Lett.*

[36] Liu Y, Hao L, Gao W, Wu Z, Lin Y, Li G, Guo W, Yu L, Zeng H, Zhu J and Zhang W 2015 Hydrogen gas sensing properties of MoS2/Si heterojunction *Sensors Actuators, B Chem.*